The Journal of Chemical Physics

# Multimode two-dimensional vibronic spectroscopy. I. Orientational response and polarization-selectivity

Cite as: J. Chem. Phys. **154**, 184201 (2021); https://doi.org/10.1063/5.0047724
Submitted: 16 February 2021 • Accepted: 19 April 2021 • Published Online: 11 May 2021

James D. Gaynor, Robert B. Weakly and Munira Khalil



AIP Publishing

The Journal of Chemical Physics ARTICLE scitation.org/journal/jcp

# Multimode two-dimensional vibronic spectroscopy. I. Orientational response and polarization-selectivity

Cite as: J. Chem. Phys. 154, 184201 (2021); doi: 10.1063/5.0047724
Submitted: 16 February 2021 • Accepted: 19 April 2021 •
Published Online: 11 May 2021



James D. Gaynor,[a] Robert B. Weakly, and Munira Khalil[b]

## AFFILIATIONS

Department of Chemistry, University of Washington, P.O. Box 351700, Seattle, Washington 98195, USA

**Note:** This paper is part of the JCP Special Topic on Coherent Multidimensional Spectroscopy.
[a]**Current address:** Department of Chemistry, University of California, Berkeley, California 94720, USA.
[b]**Author to whom correspondence should be addressed:** mkhalil@uw.edu

## ABSTRACT

Two-dimensional Electronic–Vibrational (2D EV) spectroscopy and two-dimensional Vibrational–Electronic (2D VE) spectroscopy are among the newest additions to the coherent multidimensional spectroscopy toolbox, and they are directly sensitive to vibronic couplings. In this first of two papers, the complete orientational response functions are developed for a model system consisting of two coupled anharmonic oscillators and two electronic states in order to simulate polarization-selective 2D EV and 2D VE spectra with arbitrary combinations of linearly polarized electric fields. Here, we propose analytical methods to isolate desired signals within complicated spectra and to extract the relative orientation between vibrational and vibronic dipole moments of the model system using combinations of polarization-selective 2D EV and 2D VE spectral features. Time-dependent peak amplitudes of coherence peaks are also discussed as means for isolating desired signals within the time-domain. This paper serves as a field guide for using polarization-selective 2D EV and 2D VE spectroscopies to map coupled vibronic coordinates on the molecular frame.



## I. INTRODUCTION

The seminal work of Aue and co-workers[1] laid a foundation for the development of multidimensional Fourier-transform (FT) spectroscopy, first using pulses in the radio frequency spectral region to map correlated nuclear spin phenomena. In the decades since, advancements in laser technology have enabled a spectral exploration of this technique, which now reaches throughout the terahertz, mid-infrared, visible, and ultraviolet spectral regions.[2] Coherent multidimensional spectroscopy is now capable of measuring chemical dynamics occurring on the femtosecond (fs) and picosecond (ps) timescales, in non-equilibrated ground and excited states that have complex molecular couplings between many different degrees of freedom.

Two-dimensional electronic spectroscopy (2D ES) and two-dimensional infrared spectroscopy (2D IR) are well-established coherent multidimensional techniques that are used extensively to investigate chemical and physical processes in the condensed phase. An effective probe of electronic couplings, 2D ES, has been critical for understanding photosynthetic energy transfer,[3–8] charge transfer,[9] excitonic phenomena,[10–12] and quantum coherences in dimers and aggregates.[13–15] The sensitivity of vibrations to molecular structural parameters has made 2D IR an essential tool for measuring chemical exchange,[16–18] vibrational anharmonicity and couplings,[19–23] spectral diffusion in liquids,[24–28] and structural dynamics in proteins.[29–34] Incorporating polarization-selectivity into 2D ES and 2D IR experiments has significantly enhanced our ability to obtain molecular-frame structural insight and to deconvolve congested spectra. By experimentally controlling the polarization of the three incident electric fields and the detected signal field, specific transition dipole moments can be isolated and cross peaks describing interactions between different dipole moments can be enhanced.[35–38] In 2D ES, polarization-selectivity can distinguish different electronic states through its sensitivity to the orientation of

the dipole moment.[3,37,39] In some instances, polarization-selective 2D ES has also been able to map observed electronic dynamics onto specific vibrational coordinates.[40,41] Polarization-selective 2D IR spectroscopy can be used to measure angles between coupled vibrational coordinates,[42–45] to extract hydrogen bond jump angles during chemical exchange,[46] to observe reorientation-induced spectral diffusion,[47] and to determine the secondary protein structure.[48] The 2D IR and 2D ES techniques are primarily sensitive to correlated dynamics involving vibrational and electronic motion, respectively. Direct measurements of correlated motion involving both electronic and vibrational degrees of freedom—known as vibronic couplings—requires resonant techniques that interact with both electronic and vibrational transitions.

Two-dimensional Electronic–Vibrational (2D EV) spectroscopy and two-dimensional Vibrational–Electronic (2D VE) spectroscopy are among the most recent additions to the coherent multidimensional spectroscopy toolbox.[49–52] These multicolor, coherent FT techniques include both electronically resonant interactions in the UV–visible spectral domain and vibrationally resonant interactions in the mid-infrared domain (see Fig. 1 pulse sequences) and are uniquely sensitive to vibronic coupling.[53] Recent 2D EV and 2D VE investigations have produced new insight into ultrafast charge transfer in transition metal complexes,[54–57] proton transfer,[58] photosynthetic light-harvesting,[59–62] and dynamics at conical intersections.[63,64] Polarization-selectivity has also been experimentally incorporated into both techniques to better understand congested spectra[54,59] and separate orientational response from the vibronic molecular response.[57] Theoretical treatments are actively developing an infrastructure to fully understand the information content of the measured spectra for model systems including one vibronically coupled anharmonic oscillator on two electronic states,[53] a vibronically coupled molecular dimer containing a vibrational frequency resonant with the excitonic energy gap,[65] and investigations into the origin of 2D EV line shapes.[66–68] Of particular interest for ultrafast excited state phenomena is the role those vibronic couplings, non-Condon effects, and Duschinsky mixing play in

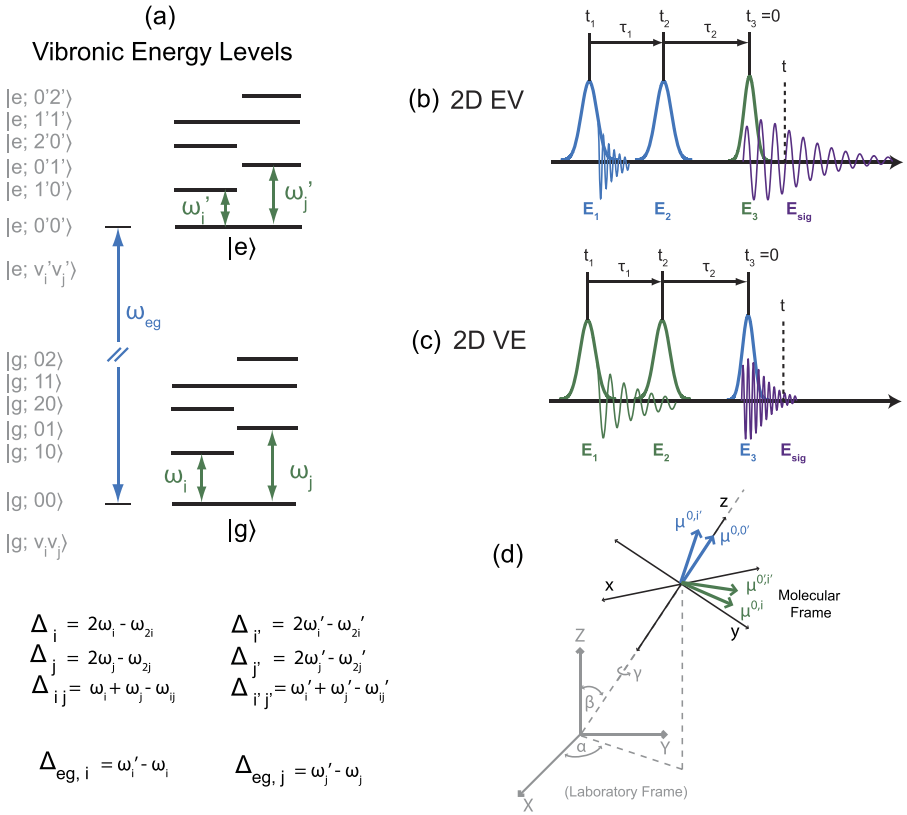


**FIG. 1**. 2D spectroscopy overview of a multimode vibronic system. The vibronic eigenstates of a coupled multimode molecular system are shown schematically in (a) where the electronic state (e) or (g) and the vibrational quanta ($v_i$ and $v_j$) of the two coupled oscillators, *i* and *j*, are specified by $|g; v_i, v_j\rangle$ and $|e; v_{i'}, v_{j'}\rangle$; primes indicate electronically excited state vibrations. Analytical expressions for eigenstate separation are also given. Experimental pulse sequences for (b) 2D Electronic–Vibrational (2D EV) and (c) 2D Vibrational–Electronic (2D VE) spectroscopies are shown; the four electric fields are denoted $\boldsymbol{E}_1$, $\boldsymbol{E}_2$, $\boldsymbol{E}_3$, and $\boldsymbol{E}_{sig}$, with corresponding wavevectors $\boldsymbol{k}_1$, $\boldsymbol{k}_2$, $\boldsymbol{k}_3$, and $\boldsymbol{k}_{sig}$ (blue = electronically resonant, green = vibrationally resonant, and purple = signal). The molecular orientation within the laboratory frame is exemplified in (d) using dipole moments for oscillator *i* for the electronic ($\boldsymbol{\mu}^{0,0'}$, $\boldsymbol{\mu}^{0,i'}$) and vibrational ($\boldsymbol{\mu}^{0,i}$, $\boldsymbol{\mu}^{0',i'}$) transitions. The relative angles of these dipole moments can be accessed experimentally as well as all other combinations of dipole moments contributing to any of the quantum transition pathways in either 2D spectroscopy. See text for definitions of dipole moments. The molecular frame basis vectors are in lower case ($\hat{x}, \hat{y}, \hat{z}$), while the laboratory frame basis vectors are in upper case ($\hat{X}, \hat{Y}, \hat{Z}$).

determining relaxation trajectories.[41,69–75] By exploiting direct sensitivity to both electronic and vibrational motions, 2D EV and 2D VE spectroscopies are well-suited for such investigations. Other works have used the term "vibronic" to describe strong coupling between multiple excited electronic states.[65,70] Here, the term is used to explicitly describe a ground and single excited state coupling through the vibrational modes of interest in the weak coupling limit. This paper is the first in a series of two papers that investigates the 2D EV and 2D VE spectral signatures of a model system involving two vibronically coupled anharmonic vibrations in two electronic states, but it is readily extendable to multiple vibrational modes. We leave the inclusion of multiple excited electronic states for a future publication. For brevity, we will collectively refer to both 2D EV and 2D VE spectroscopies as 2D "vibronic" spectroscopies.

The emphasis in this Paper I is on the nonlinear orientational response of the model system with generally defined vibronic system eigenstates. A complete treatment of the vibronic system Hamiltonian is reserved for Paper II in this series,[76] which provides a detailed account of how non-Condon effects, the Huang–Rhys parameter,[77,78] and Duschinsky mixing are measured in the 2D vibronic spectra for this specific multimode system.

This paper is organized as follows: Sec. II briefly outlines the model system discussed here and introduces the nonlinear orientational response. In Sec. III, the 2D Vibronic peak positions, amplitudes, and line shapes are discussed, and a nomenclature is developed to facilitate the discussion of the 2D vibronic spectra such that each of the contributing transition pathways and the involved transition dipole moments in each polarization-selective 2D spectrum can be specified. The system–bath interactions for this model system are treated in the homogeneous dephasing limit. Section IV treats the orientational response functions within the framework of orientational diffusion, assuming that the dipole moments behave as symmetric diffusers in isotropic media, and gives expressions for the generalized 2D vibronic nonlinear orientational response functions. After constructing the complete set of response functions, the orientational responses for polarization-selective signals are calculated in Sec. V and observables such as spectral anisotropy and the depolarization ratio are derived and discussed. The orientational response of 2D vibronic spectroscopies inherently contains angular dependence of at least one angle and can have up to four angles in the framework discussed here. Section VI extends the discussion of the polarization-selective 2D Vibronic spectroscopic observables. Importantly, new insights from a systematic anisotropy analysis are shown, which can involve multiple peaks measured in either one of these techniques. Furthermore, anisotropy ratios between specific vibronic pathways in both spectroscopies increase the set of dipole moments whose relative orientations can be determined. In principle, this systematic analysis could directly identify and quantify the presence of non-Condon effects and Duschinsky mixing. Comparisons between 2D vibronic spectral observables and those of other ultrafast spectroscopies are then made to contextualize the capabilities of these newer techniques. Specific polarization schemes are discussed, which can help to selectively enhance particular pathways of interest when spectra are congested with overlapping features. Finally, we discuss how time dependence can be used to deconvolve the complete third-order vibronic response probed in 2D vibronic spectroscopies. One goal of this paper is for this discussion to serve as a field guide for other researchers wishing to perform polarization-selective 2D vibronic experiments on more widely varied molecular systems. Finally, Sec. VII concludes Paper I of this two-part series and introduces Paper II.[76]

## II. POLARIZATION-SELECTIVE THIRD-ORDER 2D VIBRONIC SPECTROSCOPY: A MODEL MULTIMODE SYSTEM

The multimode vibronic system considered in this paper consists of two coupled anharmonic vibrational coordinates, $i$ and $j$, in two different electronic states, $|g\rangle$ and $|e\rangle$. The vibronic couplings result in excited state displacement along vibrational coordinates, vibrational frequency shifting, and vibrational mode mixing (known as Duschinsky mixing). Generalized eigenstates for such a model system are depicted in Fig. 1(a) along with analytical expressions for the energy separations of the eigenstates. The electronic ground and excited eigenstates are specified by $|g;v_i,v_j\rangle$ and $|e;v_{i'},v_{j'}\rangle$, respectively, where primes denote electronically excited state vibrations. The pulse sequences for the 2D EV and 2D VE spectroscopies are given in Figs. 1(b) and 1(c), where the electronically resonant and vibrationally resonant electric fields are identified in blue and green, respectively.

In the limit that the orientational dynamics such as rotational diffusion occur on much slower timescales than vibronic dynamics of a molecule in solution, the complete third-order material response tensor ($\overleftrightarrow{\boldsymbol{R}}^{(3)}$) may be expressed as the product of the orientational response tensor ($\overleftrightarrow{\boldsymbol{Y}}$) and the vibronic response ($\boldsymbol{R}$).[36,79,80] The third-order material response function consists of eight distinct Liouville pathway types that group into four pairs of complex conjugate field–matter interaction pathways. Therefore, summing over all possible third-order transition pathways, $\alpha$, $\overleftrightarrow{\boldsymbol{R}}^{(3)}$ is expressed as

$$\overleftrightarrow{\boldsymbol{R}}^{(3)}(\tau_3,\tau_2,\tau_1)=\sum_{\alpha=1}^{4}\sum_{IJKL}\sum_{a,b,c,d}(Y_\alpha)_{IJKL}^{abcd}(\tau_3,\tau_2,\tau_1)R_\alpha^{abcd}(\tau_3,\tau_2,\tau_1). \tag{1}$$

The nonlinear tensorial orientational response $Y_{IJKL}^{abcd}(\tau_3,\tau_2,\tau_1)$, which specifies elements of the generalized orientational tensor ($\overleftrightarrow{\boldsymbol{Y}}$), accounts for sequential projections of the four linearly polarized electric fields in the fixed laboratory frame onto the fixed molecular frame for each successive field–matter interaction. The indices (a–d) denote the vibronic eigenstates involved in each pathway as defined by a vibronic system Hamiltonian. The time dependence of $Y_{IJKL}^{abcd}(\tau_3,\tau_2,\tau_1)$ includes the molecular diffusion between field–matter interactions. The indices $[I,J,K,L]\in[X,Y,Z]$ are a permutation of the electric field polarization over the laboratory frame coordinates (X, Y, Z).

The third-order response function for 2D vibronic spectroscopies measures the couplings between vibronic and vibrational transition dipole moments [see Fig. 1(d)]. These transition dipole moments describe either vibronic transitions, where changes in both the electronic state and vibrational state can occur, or vibrational transitions occurring in the same electronic state. An illustration of the molecular transition dipole moments that can be selectively probed in a polarization-selective 2D vibronic spectroscopy is given in Fig. 1(d) using oscillator $i$ as an example. It is the interaction

Hamiltonian, $H_{int} = -\boldsymbol{M}\cdot\boldsymbol{E}(\boldsymbol{k}, \omega, t)$, that explicitly describes the light–matter interaction itself, where the transition dipole operator is $\boldsymbol{M}$ and the time-dependent electric field is defined by its wavevector, $\boldsymbol{k}$, and its angular carrier frequency, $\omega$. The system dipole operator is defined in terms of the vibronic system eigenstates [$|a(r,Q)\rangle$ and $|b(r,Q)\rangle$], and the transition dipole moment matrix element between eigenstates $a$ and $b$ is given by $\mu^{a,b}$. Here, the generalized vibronic eigenstates are written as functions of the electron coordinates, $r$, and the nuclear coordinates, $Q$. The transition dipole moment vector connecting eigenstates $a$ and $b$ is represented by $\boldsymbol{\mu}^{a,b} = \hat{\mu}^{a,b} \times \mu^{a,b}$; that is, the dipole moments possess a direction in the molecular frame, expressed by the unit vector $\hat{\mu}^{a,b}$, as well as the magnitude of the dipole moment expressed by $\mu^{a,b}$. Therefore, $H_{int}$ can be written as

$$H_{int} = (\hat{\mu}^{a,b}\cdot\hat{E}_Z)\times(\mu^{a,b}e^{i(\boldsymbol{k}\cdot\hat{X}-\omega t)}) \tag{2}$$

for the light–matter interaction of an electric field propagating along in the $\hat{X}$ direction with a linear polarization in the $\hat{Z}$ direction of the laboratory frame that is defined by the vector $\hat{E}_Z$. The first part of Eq. (2) containing the scalar product is related to the nonlinear orientational response, while the second part is related to the nonlinear vibronic response through the transition probability between the system eigenstates given the spectral intensity of the incident electric fields. As previously shown for a single mode case,[53] expanding the dipole moment operator to explicitly treat the electronic and vibrational transitions that are probed in these spectroscopies demonstrates the direct sensitivity to the measurement of non-Condon effects and electrical anharmonicity. For example, both 2D EV and 2D VE spectroscopies have access to vibronic transition dipole moments that only affect the electronic state ($|g;00\rangle \leftrightarrow |e;0'0'\rangle$) and to those that affect both the electronic and vibrational degrees of freedom ($|g;00\rangle \leftrightarrow |e;1'0'\rangle$). The development of a vibronic Hamiltonian resulting in the vibronic eigenstates shown in Fig. 1(a) and the connection between vibronic coupling parameters and the relative orientations of the vibronic transition dipole moments shown in Fig. 1(d) are detailed in Sec. III of Paper II of this series.[76]

In this work, we employ a simplified transition dipole moment notation for $\boldsymbol{\mu}^{a,b}$: a prime denotes the excited electronic state (no prime indicates the ground state), superscript index 0 indicates the common ground state (zero quanta of each oscillator), and the superscript index $i$, $j$, or $ij$ specifies the vibrational quanta in either $i$, $j$, or a common state with nonzero vibrational quanta in each oscillator, respectively. For example, the fundamental electronic transition $\boldsymbol{\mu}^{|g;00\rangle,|e;0'0'\rangle}$ is expressed as $\boldsymbol{\mu}^{0,0'}$, and $\boldsymbol{\mu}^{|g;10\rangle,|e;1'1'\rangle} \equiv \boldsymbol{\mu}^{i,i'j'}$. The angle between the two dipole moments $\boldsymbol{\mu}^{a,b}$ and $\boldsymbol{\mu}^{c,d}$ is denoted $\theta^{c,d}_{a,b}$ using the same simplified notation for the transition dipole moments. For example, the angle formed between $\boldsymbol{\mu}^{0,0'}$ and $\boldsymbol{\mu}^{0,i}$ is defined $\theta^{0,i}_{0,0'}$. Here, the molecular frame is defined such that $\boldsymbol{\mu}^{0,0'}$ is parallel to $\hat{z}$ with all transition dipole moments defined in the $yz$-plane; this orientation sets all dipole moments relative to $\boldsymbol{\mu}^{0,0'}$. We note that $\boldsymbol{\mu}^{0,0'}$ expresses the same dipole moment as $\boldsymbol{\mu}^{e,g}$ used previously.[53] The laboratory frame coordinates (X, Y, Z) are shown in gray with the Euler angles ($\alpha$, $\beta$, $\gamma$) that describe the relative orientation of the molecular frame and the laboratory frame. Using polarizers to control the linear polarization of the incident electric fields allows the experimentalist access to specific molecular frame orientations and dipole angles. Typical polarization combinations include the parallel configuration, in which all incident fields have linear polarization that are parallel to one another (ZZZZ), and the perpendicular (or "crossed") configuration, in which the first two electric fields are parallel to one another and the last two electric fields are rotated 90° from the first two fields (YYZZ). Many other polarization combinations have also been exploited in 2D spectroscopy to isolate specific signals.[38] Importantly, performing 2D EV and 2D VE experiments with polarization-selectivity can facilitate signal isolation in otherwise congested spectral regions and potentially separate the orientational signal contributions from the vibronic molecular signal contributions.

## III. 2D VIBRONIC SPECTRAL FEATURES: POSITIONS, AMPLITUDES, AND LINE SHAPES

Establishing a self-consistent system of reference for pathway types and peak characteristics is crucial for furthering the present discussion. Additionally, the determination of a particular vibrational mode's role in a vibronic pathway greatly aids the interpretation of the polarization-selective data as the relative orientations of vibrational modes dictate the strength of the vibronic response. This section should be used as an informative reference in denoting pathways for both EV and VE spectroscopy throughout both papers in this series. Each peak measured in a 2D EV or 2D VE spectrum of a multimode system reports on the simultaneous contribution of multiple vibronic pathways with overlapping spectral locations. Each pathway may be described by a symbol written as

$$\mathrm{N}^{m_3}_{m_1,m_2} \tag{3}$$

for pathway types N, where $\mathrm{N} \in \mathrm{I} - \mathrm{VII}$, and vibrational indices $m_1, m_2, m_3$. The pathway labels in the Feynman diagrams of Figs. 2 and 3 connote the type of signal [ground state bleach (GSB), excited state absorption (ESA), or excited state stimulated emission (ESE)] and a description of the transition pathway responsible for the signal. All pathways originate in the ground state as we assume the low temperature (T) limit such that one vibrational quantum is much greater than $K_BT$, where $K_B$ is the Boltzmann constant.

The two subscript values ($m_1, m_2$) denote the vibrational part of the vibronic state that is involved with the first two respective light–matter interactions. For example, in the pathway $\mathrm{VI}^{ij}_{i,j}$, $\boldsymbol{k}_1$ induces a change in vibrational quanta of mode $i$ and $\boldsymbol{k}_2$ induces a change in vibrational quanta of mode $j$. Similarly, the superscript (ij) indicates the vibrational part of the vibronic state accessed by $\boldsymbol{k}_3$. When $m_1$, $m_2$, or $m_3$ are equal to zero, this indicates that the light–matter interaction has brought the system to the lowest energy eigenstate (e.g., $|g;00\rangle$ or $|e;0'0'\rangle$). Importantly, this labeling scheme is generalizeable to both techniques with a few exceptions detailed below. It applies to both the 2D EV and 2D VE transition pathways because the electronic part of the vibronic eigenstates is not directly specified, but rather inferred from whichever spectroscopy is being discussed. For comparison, the double-sided Feynman diagrams for pathways $\mathrm{VI}^{ij}_{i,j}$ are found in Fig. 2 for 2D EV spectroscopy and Fig. 3 for 2D VE spectroscopy. The main differences are that the $\tau_2$ coherences occur in the electronically excited state for 2D EV ($|e;1'0'\rangle\langle e;0'1'|$) and the ground state for 2D VE ($|g;10\rangle\langle g;01|$) and

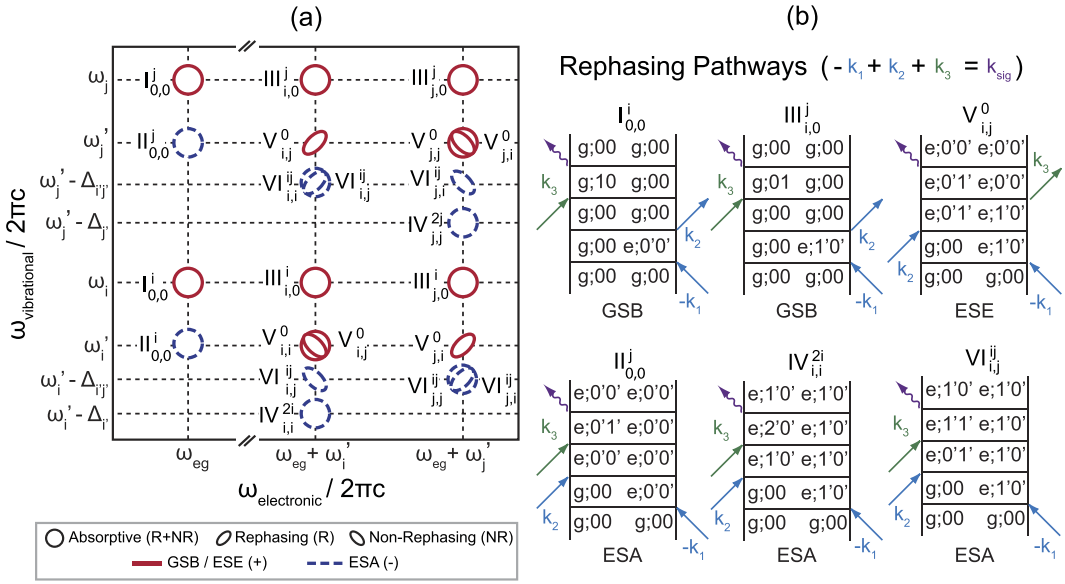


**FIG. 2**. Multimode 2D EV signals schematic. (a) A schematic illustration of the dipole allowed 2D EV signals appearing for a two-mode vibronically coupled system and the energy level schematic described in Fig. 1. The absorptive pathways are symmetric and result from equally weighted rephasing (R) and non-rephasing (NR) pathways, generating signals at the same ($\omega_1$, $\omega_3$) coordinates; phase twisted pathways result from unequally weighted R and NR signals; red = positive signal [ground state bleaches (GSB) and excited state stimulated emissions (ESE)], blue = negative signal [excited state absorptions (ESA)]. The pathway numbering scheme is described in the main text. (b) Double-sided Feynman diagrams of diagrams of selected 2D EV rephasing pathways. Electronic excitations ($\boldsymbol{k}_1$ and $\boldsymbol{k}_2$, blue), vibrational interactions ($\boldsymbol{k}_3$, green), and emitted signal ($\boldsymbol{k}_{sig}$, purple).

that the $\tau_3$ coherence period captures a purely excited state vibrational coherence in 2D EV spectroscopy ($|e;1'1'\rangle\langle e;0'1'|$), while the $\tau_3$ coherence in 2D VE spectroscopy includes the two electronic states ($|e;1'1'\rangle\langle g;01|$). It should be noted that for systems including more than one excited electronic state, 2D EV spectroscopy is also sensitive to coherences involving different electronic states.[55]

Pathway numbers I–V are simple variations of previous pathway descriptions,[53] expanded to include possible interactions with multiple modes in the cases of pathways III and V. Pathways I and II are GSBs and ESAs that have $\mu^{0,0'}$ electronic transitions, respectively; all other pathway numbers have different electronic transitions, either greater or lesser in energy than $\hbar\omega_{eg}$. Pathways III and IV are GSBs and ESAs that access higher lying vibrational levels in $|e\rangle$, respectively. Notably, the two spectroscopies differ in the definition of pathways V. The 2D EV transition pathways include excited state stimulated emissions for pathways labeled V; 2D VE transition pathways do not permit stimulated emissions, and so pathways V are ESAs with electronic transitions between states with smaller energy gaps than $\hbar\omega_{eg}$. Pathways VI are the ESAs that access the shared vibrational state $|e;1'1'\rangle$, either through a coherence or population in $\tau_2$. Pathways VII only occur in 2D VE spectroscopy and are defined by the electronic transition driving a change of vibrational quanta in both modes ($\Delta_{\nu_i} = -\Delta_{\nu_j}$). In general, a $\tau_2$ coherence is indicated by any pathway in which $m_1 \neq m_2 \neq 0$.

Since the electronic information is not directly included in the pathway labeling scheme, a few important labeling distinctions between 2D EV and 2D VE pathways should be noted. First, the set of allowed transitions in 2D EV spectroscopy includes the case where $m_1 = m_2 = 0$, whereas the 2D VE pathways are such that $m_1$ and $m_2$ can never both equal 0. As a result, all pathways in 2D VE spectroscopy are uniquely described by label subscripts and superscripts. However, knowledge of the path type N may be required to distinguish the 2D EV pathway. For example, any 2D VE pathway in which $m_2 = 0$ denotes a GSB, while the 2D EV pathway $N^i_{0,0}$ would reference a GSB (N = I) or an ESA (N = II).

The principal aim of this paper is to account for the signal amplitude arising from the directionality of the dipole moments by using polarization-selective light–matter interactions in these 2D vibronic spectroscopies. The nature of the signatures measureable in 2D vibronic spectra will be introduced in the remainder of this section. 2D vibronic orientational response and polarization-selectivity are then fully addressed in beginning in Sec. IV after this groundwork has been established.

### A. 2D Electronic-Vibrational signatures

A cartoon schematic of an absorptive 2D EV spectrum for a multimode molecular system is shown in Fig. 2. The pathways depicted are those that would arise from electronically resonant electric fields ($\boldsymbol{E}_1$ and $\boldsymbol{E}_2$) with center frequency $\omega_{eg}$ and bandwidth $2\omega_j$ to allow resonant transitions into higher lying vibrational states of both the vibrational coordinates $Q_i$ and $Q_j$ (where $\omega_i < \omega_j$). The vibrationally resonant field ($\boldsymbol{E}_3$) is assumed to have sufficient bandwidth to excite one-quantum transitions only and spans the vibrational transition frequencies of interest. The fully absorptive spectrum results from the sum of the rephasing (R, $\boldsymbol{k}_{sig} = -\boldsymbol{k}_1 + \boldsymbol{k}_2 + \boldsymbol{k}_3$)

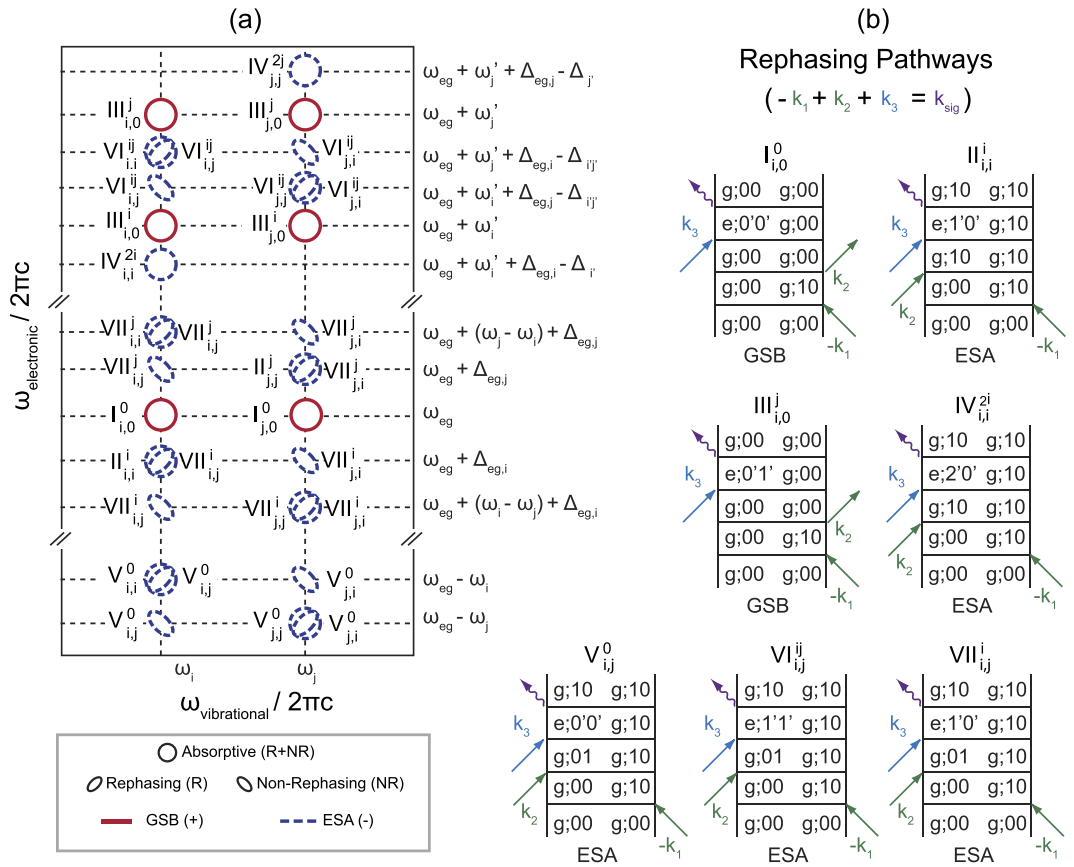


**FIG. 3**. Multimode 2D VE signals schematic. (a) A schematic illustration of the dipole allowed 2D VE signals appearing for a two-mode vibronically coupled system and the energy level schematic given in Fig. 1. The absorptive pathways are symmetric and result from equally weighted rephasing (R) and non-rephasing (NR) pathways, generating signals at the same ($\omega_1$, $\omega_3$) coordinates; phase twisted pathways result from unequally weighted R and NR signals; red = positive signal [ground state bleaches (GSB)], blue = negative signal [excited state absorptions (ESA)]. The pathway numbering scheme is described in the main text. (b) Double-sided Feynman diagrams of selected 2D VE rephasing pathways. Vibrational excitations ($\boldsymbol{k}_1$ and $\boldsymbol{k}_2$, green), electronic interactions ($\boldsymbol{k}_3$, blue), and emitted signal ($\boldsymbol{k}_{sig}$, purple).

and non-rephasing (NR, $\boldsymbol{k}_{sig} = +\boldsymbol{k}_1 - \boldsymbol{k}_2 + \boldsymbol{k}_3$) signal pathways, which differ by the phase of the oscillation propagating during the $\tau_1$ coherence period. When a R and NR signal pathway with the same ($\omega_1$, $\omega_3$) coordinates are equally weighted and the dynamics can be described within the homogeneous limit, their sum results in a symmetric pathway without any phase twist, as shown in Fig. 2 (e.g., pathway $I^{j}_{0,0}$). Likewise, pathways arising from unequally weighted R and NR contributions will result in elongated features with either positive (R) or negative (NR) slopes.

The specific pathway positions correspond to the transition frequencies between vibronic eigenstates of the molecular system being studied. In general, a system Hamiltonian determines the nature of the eigenstates for the system of interest. In this discussion, the vibronic system consists of two electronic states (the ground $g$ and excited $e$ states) and two coupled anharmonic vibrations whose frequencies and couplings change in the excited state. As shown in Fig. 2 (and Fig. 3 for 2D VE), the frequency separations of the pathways are expressed as a combination of system transition frequencies $\omega$ and energy shifts $\Delta$ (with appropriate indices, defined in Fig. 1) resulting from the system Hamiltonian. A 2D EV spectrum of a two-mode system includes two blocks of pathways I–V corresponding to each of the vibrational modes (e.g., the $i$th mode pathways: $I^{i}_{0,0}$; $II^{i}_{0,0}$; $III^{i}_{i,0}$; $IV^{i}_{i,i}$; $V^{i}_{i,i}$). Each of these pathways has equal R and NR contributions that evolve as a decaying population during $\tau_2$. The electronic excitations to $|e;0'0'\rangle$ will appear at $\omega_1 = \omega_{eg}$, and the oscillator $i$ excitations to $|e;1'0'\rangle$ will have $\omega_1 = \omega_{eg} + \omega_{i'}$ coordinates; the oscillator $j$ excitations follow similarly. New pathways also appear due to the system including two coupled vibrational modes from pathways utilizing the shared vibrational states $|g;00\rangle$, $|e;0'0'\rangle$, and $|e;1'1'\rangle$. These pathways are distinguished by the first two light–matter interactions involving one vibration and the third light–matter interaction involving a different vibration, and they also have matched R and NR pathways (e.g., $III^{i}_{j,0}$). Additional pathways that excite different vibrations during the $\boldsymbol{k}_1$ and $\boldsymbol{k}_2$ interactions result in $\tau_2$ coherences. The phase matching conditions necessarily separate

the R and NR pathways spectrally (e.g., $V^{0}_{j,i}$; $V^{0}_{j,i}$; $VI^{ij}_{i,j}$; $VI^{ij}_{j,i}$) resulting in phase twisted line shapes; see the supplementary material for a comparison of R and NR signal pathways.

The amplitudes of the 2D EV pathways are dependent on the ground state population of molecules (i.e., in $|g;00\rangle\langle g;00|$, assumed to be all molecules in this work) and the strength of the four transition dipole moments accessed by the field–matter interactions during a vibronic transition pathway. The explicit treatment of the electronic and vibrational transition dipole moments in the interaction Hamiltonian incorporate the nuclear dependence of the electronic transition and the electrical anharmonicity of a vibration in an excited electronic state; a complete description of dipole moments within $H_{vibronic}$ can be found in Sec. III A of Part II of this series.[76] Not only are the signal amplitudes governed by the magnitude of the electronic and vibrational dipole moments, but the vectorial nature of the dipole moments in the molecular frame contributes amplitude that depends upon their relative orientation with each other and with the incident electric fields.

Spectral line shapes in the homogeneous dephasing limit are based on the analytical expressions for energy gap correlation functions used in previous work[53] and follow the work of Sung and Silbey.[79] Here, they have been expanded to include multimode effects and are reported in the supplementary material. Recent investigations into inhomogeneous line shapes and dynamics of 2D EV peaks may be found elsewhere.[68] Interestingly, the correlated (or anti-correlated) line shapes may occur in a multimode 2D EV spectrum even within the homogeneous limit as a result of spectrally separated R and NR pathways with respect to $\omega_3$ in the 2D spectrum. For example, consider pathway $VI^{ij}_{i,j}$ that has a positively correlated line shape when $\tau_2$ is such that the $|e;0'1'\rangle\langle e;1'0'|$ coherence is constructively interfering. As discussed above, these contributions will necessarily oscillate at the $|\omega_{j'} - \omega_{i'}|$ difference frequency producing a dynamic center line slope across the bandwidth of this feature. The spectral resolution of the pathways with this dynamic is inherently linked to the magnitude of $\Delta_{i'j'}$ because the oppositely signed ESE, $V^{0}_{i,j}$, will have the same oscillatory behavior and can cancel out part of the dynamic signal in pathway $VI^{ij}_{i,j}$ if $\Delta_{i'j'}$ does not sufficiently separate these two pathways in the $\omega_3$ dimension. Section II C of Paper II[76] connects the $\Delta_{i'j'}$ splitting to the Duschinsky mixing.

## B. 2D Vibrational-Electronic signatures

A cartoon schematic of an absorptive 2D VE spectrum and corresponding Feynman pathways are shown in Fig. 3. The pathways depicted meet analogous criteria as those listed above for 2D EV. The 2D VE spectrum assumes the same spectral properties of the electronically and vibrationally resonant electric fields as described above for 2D EV. However, the temporal ordering of these electric fields are opposite in the 2D VE experiment, where $\boldsymbol{E}_1$ and $\boldsymbol{E}_2$ are vibrationally resonant and $\boldsymbol{E}_3$ is electronically resonant. The 2D VE schematic shows pathways associated with the vibronic eigenstates shown in Fig. 1(a) and demonstrates the same organization of R and NR pathways; for example, pathway $V^{0}_{i,i}$ is symmetric, while pathways $V^{0}_{i,j}$ have spectrally separated, positively (negatively) sloped R (NR) components.

The $\omega_1$ pathway positions are determined by the first light–matter interaction, which resonantly excites a vibrational transition in oscillator $i$ or $j$ yielding pathways centered at $\omega_1 = \omega_i$ or $\omega_j$. The probed $\omega_3$ positions are determined by the frequencies of the final vibronic transitions. Hence, the $\omega_3$ pathway positions in 2D VE spectroscopy contain the information regarding the vibrational structure of excited electronic states. Several pathways arise from the participation of multiple vibrational modes as shown in Fig. 3. Such pathways may be observed in the probe domain with $\omega_3$ positions at different frequencies from $\omega_{eg}$, as is the case for pathway $III^{j}_{i,0}$. Another set of pathways, $VI^{ij}_{i,j}$ and $VII^{i}_{i,j}$, results from the two excitation pulses creating a vibrational coherence. With exception to pathways $IV^{2i}_{i,i}$ and $IV^{2j}_{j,j}$, the ESA features in 2D VE spectra appear in blocks of six pathways. For example, the lower energy ESA manifold consists of two pairs of R ($V^{0}_{i,j}$, $V^{0}_{j,i}$) and NR ($V^{0}_{i,j}$, $V^{0}_{j,i}$) pathways at opposite sides of the box and a pair of absorptive pathways ($V^{0}_{i,i}$, $V^{0}_{j,j}$) at two corners of the box. We note that the R pathways and the fully absorptive peaks are spectrally overlapping. The ESA blocks are identifiable by having frequency separations of $|\omega_j - \omega_i|$ between peaks in both the $\omega_1$ and $\omega_3$ dimensions. This structure arises because the $\tau_2$ coherence pathways access an identical set of vibronic states that either differ by the interaction order of $\boldsymbol{k}_1$ and $\boldsymbol{k}_2$ with respect to the vibrations or by the phase of the $\tau_1$ coherence. Each of the R and NR coherence pathway pairs [such as $V^{0}_{i,j}$ (R and NR)] interact with the same four transition dipoles, exhibit identical time-dependent behavior during $\tau_2$, and share the same orientational response functions.

The faster dephasing times of condensed phase electronic transitions result in 2D VE spectral features with typically broad line shapes with respect to $\omega_3$, yielding significant overlapping of oppositely signed features and a unique sensitivity to vibronic coupling parameters. For example, the 2D VE spectra are sensitive measurements of the Franck–Condon factors and Huang–Rhys parameters for the system of interest as we discuss in Secs. II B and V C of Paper II, specifically in Eqs. (6) and (15) and Figs. 2, 3 and 7.[76] This is especially true when the features of interest have electronic transition frequencies of $\omega_3 \geq \omega_{eg}$ because these regions of the 2D VE spectrum contain GSB features and ESA features of similar transition pathways that overlap significantly. The sign of the observed signal immediately indicates which of the Franck–Condon factors has greater magnitude. More generally, the 2D VE transition pathways access a greater variety of vibronic transitions than the 2D EV experiment because of the initial vibrational excitation used in the 2D VE technique. Hence, 2D VE can sample more of the coordinate space for the projection between the ground and excited electronic potentials.

The 2D VE line shapes also encode the same electronic-state-dependent vibrational dephasing as 2D EV spectroscopy does, and the same considerations discussed above apply here to the 2D VE discussion. However, the larger combination of vibronic transitions allowable in the 2D VE pulse sequence affords a larger sampling of energy gap correlation functions for a given molecular system. In principle, the 2D VE line shapes contain a large sampling of frequency fluctuations between ground and excited vibrational levels in both the ground and excited electronic states. For example, the 2D line shape of pathway $VI^{ij}_{i,i}$ is determined by the combination of auto-correlations and cross-correlations between many vibronic

eigenstates: the zero-point energies of the ground and excited electronic states ($\Gamma_{eg,eg}$), the ratio of the electronic-state-dependent vibrational fluctuations for both vibrations $i$ and $j$ ($\Gamma_{v_i,v_i}$, $\Gamma_{v_j,v_j}$, and the respective $\lambda_k$ proportionality constants), and the vibronic frequency fluctuations relating the electronic energy gap and the vibrational energy gaps in both electronic states ($\Gamma_{eg,v_i}$ and $\Gamma_{eg,v_j}$). A full list of analytic dephasing functions for 2D EV and 2D VE spectroscopies are given in the supplementary material.

## IV. NONLINEAR ORIENTATIONAL RESPONSE FOR 2D VIBRONIC SPECTROSCOPIES

From the initially isotropic orientational distribution of molecules in an ensemble, each linearly polarized electric field in the experimental pulse sequence selects a subset of molecules from the evolving orientational distribution. Given a combination of three incident pulses with fixed linear polarization, the orientational response for a specific transition pathway depends upon the directionality of the transition dipole moments in a fixed molecular frame. In our description of these 2D vibronic spectroscopies, we explicitly include both the electronic and vibrational coordinates in the set of transition dipole moments accessed experimentally (see Sec. III and Fig. 3 of Paper II in this series[76]). Thus, the orientational response for a particular vibronic transition pathway is calculated by defining the orientation of the four time-ordered vibronic transition dipole operators within the molecular frame and performing an orientational average to transform the motion of the molecular frame into the laboratory frame.

The orientational response function, $(Y_\alpha)^{a,b,c,d}_{IJKL}$, can be described within the framework of orientational diffusion. The orientational response is represented as the product of the directional cosines for all four molecular dipole moments ($\hat{\mu}$) and the molecular frame basis vectors ($\hat{i}, \hat{j}, \hat{k}$, and $\hat{l}$), which is scaled by an orientational average ($\widetilde{Y}^{ijkl}_{IJKL}$). The solutions to orientational diffusion equations and the accompanying conditional probability functions are well known,[21,81,82] and the resulting analytical expressions are given in Eqs. (4a)–(4d) for use in calculating $Y^{abcd}_{IJKL}(\tau_3,\tau_2,\tau_1)$. These factors transform the molecular orientational diffusion into the laboratory frame.

For a specific transition pathway involving four vibronic eigenstates ($a, b, c, d$), the orientational response is determined by expressing the orientation of the four involved transition dipole moments in a fixed molecular frame, projecting each transition dipole moment onto the molecular frame basis vectors ($\hat{i},\hat{j},\hat{k},\hat{l} \in \hat{x},\hat{y},\hat{z}$), and then selecting the set of laboratory frame polarization directions of the incident electric fields ($\hat{I},\hat{J},\hat{K},\hat{L} \in \hat{X},\hat{Y},\hat{Z}$) over which to orientationally average,

$$(Y_1)^{a,b,c,d}_{IJKL}(\tau_3,\tau_2,\tau_1) = \sum_{ijkl} \widetilde{Y}^{ijkl}_{IJKL}(\tau_3,\tau_2,\tau_1)\left[\hat{\mu}^{c,d}\cdot\hat{i}\right] \times \left[\hat{\mu}^{b,c}\cdot\hat{j}\right]\left[\hat{\mu}^{a,b}\cdot\hat{k}\right]\left[\hat{\mu}^{d,a}\cdot\hat{l}\right], \quad (4a)$$

$$(Y_2)^{a,b,c,d}_{IJKL}(\tau_3,\tau_2,\tau_1) = \sum_{ijkl} \widetilde{Y}^{ijkl}_{IJKL}(\tau_3,\tau_2,\tau_1)\left[\hat{\mu}^{c,b}\cdot\hat{i}\right] \times \left[\hat{\mu}^{d,c}\cdot\hat{j}\right]\left[\hat{\mu}^{b,a}\cdot\hat{k}\right]\left[\hat{\mu}^{a,d}\cdot\hat{l}\right], \quad (4b)$$

$$(Y_3)^{a,b,c,d}_{IJKL}(\tau_3,\tau_2,\tau_1) = \sum_{ijkl} \widetilde{Y}^{ijkl}_{IJKL}(\tau_3,\tau_2,\tau_1)\left[\hat{\mu}^{c,b}\cdot\hat{i}\right] \times \left[\hat{\mu}^{b,a}\cdot\hat{j}\right]\left[\hat{\mu}^{d,c}\cdot\hat{k}\right]\left[\hat{\mu}^{a,d}\cdot\hat{l}\right], \quad (4c)$$

$$(Y_4)^{a,b,c,d}_{IJKL}(\tau_3,\tau_2,\tau_1) = \sum_{ijkl} \widetilde{Y}^{ijkl}_{IJKL}(\tau_3,\tau_2,\tau_1)\left[\hat{\mu}^{a,b}\cdot\hat{i}\right] \times \left[\hat{\mu}^{b,c}\cdot\hat{j}\right]\left[\hat{\mu}^{c,d}\cdot\hat{k}\right]\left[\hat{\mu}^{d,a}\cdot\hat{l}\right]. \quad (4d)$$

Equations (4a)–(4d) differ only by the ordering of vibronic eigenstates interacting with the electric fields, as labeled by $\alpha$. Typically, orientational diffusion timescales are much longer than the vibronic dynamics of interest, so the orientational parts of the response function can be simplified even further[36,42] to facilitate calculations of the orientational response measurable with 2D EV and 2D VE spectroscopies.

By assuming that orientational dynamics are sufficiently slow with respect to $\tau_1$, $\tau_2$, and $\tau_3$, we remove the time dependence of the orientational response, written in the examples given in Eqs. (12) and (13). Further discussion of anisotropic diffusion[82] non-diffusive orientational dynamics,[83] the scrambling of the orientational response due to vibronic coherence and population transfer processes,[84] and orientational relaxation occurring on the timescale of vibronic dynamics can be found elsewhere.[36,42,85]

## V. ANISOTROPY

The polarization-selective signals for specific 2D EV and 2D VE pathways may be calculated using Eq. (1), where the multimode vibronic response, $R^{abcd}_\alpha(\tau_3,\tau_2,\tau_1)$, is determined by the physics of the system of interest, and the orientational response, $(Y_\alpha)^{a,b,c,d}_{IJKL}$, is detailed in Sec. IV above. The 2D signals for parallel and perpendicular polarized experiments on the multimode vibronic systems can now be calculated directly, as well as any other arbitrary polarization combination. In this section, generalized analytical relationships are given for the orientational responses with varying degrees of angular dependence. The orientational responses generally can include angular dependence of one, two, and four angles. In contrast to 2D IR spectroscopy and other degenerate third-order techniques, 2D EV and 2D VE spectroscopies do not include transition pathways involving four interactions with the same transition dipole moment. Therefore, each 2D EV and 2D VE pathway must possess angular dependence on at least one angle between electronic and vibrational dipole moments, albeit $\theta = 0°$, corresponding to parallel with $\boldsymbol{\mu}^{0,0'}$, is fully allowed. Using these expressions, specific polarization-selective signals can be simulated and meaningful parameters such as the depolarization ratio and the anisotropy parameter can be derived.

The general expression for the orientational response functions for parallel [$\boldsymbol{Y}_{ZZZZ}(\theta_1)$] and perpendicular [$\boldsymbol{Y}_{YYZZ}(\theta_1)$] polarized signals of 2D vibronic signals with a single angle dependence are given in Eqs. (5) and (6).That is, $\boldsymbol{Y}_{YYZZ}$ represents the result for Eq. (4) for which the laboratory frame polarization of electric fields $[\hat{I},\hat{J},\hat{K},\hat{L}] = [\hat{Y},\hat{Y},\hat{Z},\hat{Z}]$,

$$\boldsymbol{Y}_{ZZZZ}(\theta_1) = \frac{1}{15}\left[2cos^2(\theta_1)+1\right], \quad (5)$$

$$\boldsymbol{Y}_{YYZZ}(\theta_1) = \frac{1}{15}\left[2-\cos^2(\theta_1)\right]. \quad (6)$$

Signals that depend on one angle will result from transition pathways where interactions of $\boldsymbol{k}_1$ and $\boldsymbol{k}_2$ access the same transition dipole moment, which is separate from the same transition dipole moment accessed by the interactions of $\boldsymbol{k}_3$ and $\boldsymbol{k}_{sig}$. Thus, the angle between the dipole moments accessed by $\boldsymbol{k}_2$ and $\boldsymbol{k}_3$ is the one on which the orientational response depends, and it is distinguished by the vibrational character. Since it is a requirement that $\boldsymbol{k}_1$ and $\boldsymbol{k}_2$ interact with the same dipole moment for pathways with single angular dependence, these transition pathways may be GSBs or ESAs (or ESEs in 2D EV only), which evolve in a population during the $\tau_2$ evolution time period. In 2D EV spectroscopy, this is the angle between a vibrational dipole moment in either $|g\rangle$ or $|e\rangle$ and the electronic transition dipole moment. However, in 2D VE spectroscopy, this will only be the angle between a vibrational dipole moment in $|g\rangle$ and the electronic transition dipole. While the electronic transition dipole moments may explicitly include nuclear coordinate dependence in $|e\rangle$ (e.g., through linear vibronic coupling and non-Condon effects), 2D VE spectroscopy is only directly resonant with vibrational transitions in the ground electronic state through $\boldsymbol{k}_1$ and $\boldsymbol{k}_2$.

The transition pathways that depend on two dipole angles have the same requirement for $\boldsymbol{k}_1$ and $\boldsymbol{k}_2$ as the single angle pathways, but the electronic transition must be different in energy than $\hbar\omega_{eg}$. In the case of 2D EV, this occurs when a vibrationally "hot" state in $|e\rangle$ is excited and for 2D VE when an electronic excitation from a vibrational "hot" state in $|g\rangle$ occurs. The dependence on a second angle arises when the electronic transition has a dipole moment with a different vibrational character or directionality than the $|g;00\rangle \leftrightarrow |e;0'0'\rangle$ transition dipole. When this is not the case, the analytical form of the angular dependence for such pathways reduces to the expression for a single angle. The general expressions for the polarization-selective orientational response for signals with two-angle dependencies are shown in the following equations:

$$\boldsymbol{Y}_{ZZZZ}(\theta_1,\theta_2) = \frac{1}{15}[\cos(2(\theta_1-\theta_2))+2], \tag{7}$$

$$\boldsymbol{Y}_{YYZZ}(\theta_1,\theta_2) = \frac{1}{30}[3-\cos(2(\theta_1-\theta_2))]. \tag{8}$$

Orientational response functions that depend on four separate dipole moment angles arise if each light–matter interaction involves a different transition dipole moment. Necessarily, these pathways produce a coherent superposition that propagates during the $\tau_2$ evolution time. Within the multimode molecular system considered here, the electronic transition must also change the vibrational quantum numbers (i.e., $\boldsymbol{\mu}^{0,i'}$ or $\boldsymbol{\mu}^{0,j'}$) for the pathway to carry angular dependence on four dipole angles. However, a similar angular dependence may also arise in systems composed of multiple electronic excited states, which is not discussed here. The orientational response functions for pathways with four-angle dependency are

$$\begin{aligned}\boldsymbol{Y}_{ZZZZ}(\theta_1,\theta_2,\theta_3,\theta_4) = \frac{1}{15}[&\cos(\theta_1+\theta_2-\theta_3-\theta_4)\\ &+\cos(\theta_1-\theta_2+\theta_3-\theta_4)\\ &+\cos(\theta_1-\theta_2-\theta_3+\theta_4)],\end{aligned} \tag{9}$$

$$\begin{aligned}\boldsymbol{Y}_{YYZZ}(\theta_1,\theta_2,\theta_3,\theta_4) =& \frac{1}{20}[\cos(\theta_1-\theta_2+\theta_3-\theta_4)\\ &+\cos(\theta_1-\theta_2-\theta_3+\theta_4)]\\ &-\frac{1}{30}[\cos(\theta_1+\theta_2-\theta_3-\theta_4)].\end{aligned} \tag{10}$$

While a pathway involving four distinct dipole moments will have an orientational response dependent upon four angles, the analytical form of this dependence may be simplified if some of the dipole moments are parallel. Algebraically, Eqs. (9) and (10) simplify to Eqs. (7) and (8), respectively, when $\theta_1 = \theta_2$ and $\theta_3 = \theta_4$. Likewise, the orientational response is simplified to Eqs. (5) and (6) if $\theta_2 = 0$. The angular dependence for each 2D EV and 2D VE pathway as defined for the multimode vibronic system of interest considered here is given in the Appendix.

Signals collected with particular polarization dependence can be used to extract meaningful parameters such as depolarization ratios and anisotropies. While the measured signals will be dependent on both the orientational response and the vibronic response, the following discussion focuses only on the orientational response. In the pump–probe experimental geometry, the depolarization ratio for any 2D pathway can be obtained from the signals that depend on the appropriate expressions for $\boldsymbol{Y}_{ZZZZ}$ and $\boldsymbol{Y}_{YYZZ}$ in Eqs. (5)–(10) using the relation $\frac{\boldsymbol{Y}_{YYZZ}}{\boldsymbol{Y}_{ZZZZ}}$. The anisotropy parameter, $r(\theta)$, can be derived from the ratio of the anisotropic response ($\boldsymbol{Y}_{ZZZZ} - \boldsymbol{Y}_{YYZZ}$) and the isotropic response ($\boldsymbol{Y}_{ZZZZ} + 2\boldsymbol{Y}_{YYZZ}$). For pathways carrying single angle dependency, the familiar range of anisotropies of $r = 0.4$ for parallel transition dipole moments and $r = -0.2$ for orthogonal dipole moments is obtained,

$$\begin{aligned} r(\theta) &= \frac{\boldsymbol{Y}_{ZZZZ} - \boldsymbol{Y}_{YYZZ}}{\boldsymbol{Y}_{ZZZZ} + 2\boldsymbol{Y}_{YYZZ}}\\ &= \frac{1}{5}(3\cos^2(\theta) - 1).\end{aligned} \tag{11}$$

As described in Eq. (11), the angle between two different dipole moments can be extracted directly from the anisotropy. In general, the pathways that depend on a single angle are the most directly quantifiable. The correct determination of dipole angles for pathways with two- and four-angle dependencies may require a systems-of-equations approach where one or more of these angles are first determined from other pathways with fewer angle dependency or informed by other experiments. It is also important to note that a direct and accurate determination of a dipole angle from experimental spectra relies upon the pathway being fairly isolated from other spectral features in order to exclude amplitude from different transition dipoles in the calculation of $r(\theta)$. As discussed below in Sec. VI C, such a measurement of $r(\theta)$ is most direct when the orientational response is truly dependent on *one* angle since the magnitude of the isotropic response ($\boldsymbol{Y}_{ZZZZ} + 2\boldsymbol{Y}_{YYZZ}$) is not angularly independent when there exists non-zero angles between the first two dipole moments and the last two dipole moments in the transition pathway. In particular, these type of considerations matter when dealing with mismatched R and NR pathways, which should display $\tau_2$-dependent coherences. We will discuss below and in Paper II[76] how polarization-selectivity can be used creatively to enhance specific features in convoluted spectra.

## VI. DISCUSSION

Using the orientational response described above, polarization-selective features of both techniques are calculated to better understand the molecular-level information that is obtainable from 2D EV and 2D VE experiments. It is assumed in this discussion that the signal characteristics from the vibronic part of the molecular response ($R^{a,b,c,d}$) are completely determined and are effectively unity in magnitude so that the analysis of the simulated spectral features is related directly to the orientational response, $Y_{IJKL}^{abcd}$. While separating these contributions can prove challenging in practice, it is achievable. As was shown in a recent polarization-selective 2D VE study of a cyanide-bridged mixed-valence transition metal complex, both the vibronic coupling strengths and the relative orientations between a metal-to-metal charge transfer dipole moment and the dipole moments of three vibrational coordinates were determined.[57] It is important to underscore the assumption that allows us to emphasize the orientational response because, in reality, the pathway amplitudes and amplitude ratios also depend upon the scalar part of the dipole moments that include contributions from excited state displacement (linear vibronic coupling) effects, non-Condon effects, and mechanical anharmonicity effects. However, considering only the orientational response will help to identify the orientational vs vibronic origins of signals measured experimentally. We note that, in principle, there is vibrational character in the $|g;00\rangle$ and $|e;0'0'\rangle$ states due to the vibrational zero-point energies, but our analysis assumes this to be the baseline orientation for the vibronic eigenstates and that the relative orientations between these states and those containing greater vibrational quanta are the quantity of interest. This discussion builds a foundation for extracting and separating orientational and vibronic contributions to the total molecular response in 2D EV and 2D VE spectroscopy. In Paper II, we discuss how non-Condon effects and Duschinsky mixing impact the extracted angles between vibronic transition dipoles in 2D EV and 2D VE spectra.

### A. Molecular insight from 2D vibronic anisotropy analysis

In this section, a few simple examples are given for how anisotropy can be used to extract structural information relating various dipole moments in 2D vibronic spectra. First, the orientational responses for the fully absorptive (i.e., R + NR) 2D EV pathway $II^{i}_{O,O}$ are calculated where $a = |g;00\rangle$, $b = |e;0'0'\rangle$, $c = |e;1'0'\rangle$, and $d = |e;0'0'\rangle$, and $\alpha = 1$ specifies the Liouville pathway for this vibronic transition,

$$(Y_1)_{ZZZZ} = \left[\tilde{Y}^{zzzz}_{ZZZZ}(\cos^2(\theta^{0',i'}_{0,0'})) + \tilde{Y}^{yyzz}_{ZZZZ}(\sin^2(\theta^{0',i'}_{0,0'}))\right]_R + \left[\tilde{Y}^{zzzz}_{ZZZZ}(\cos^2(\theta^{0',i'}_{0,0'})) + \tilde{Y}^{yyzz}_{ZZZZ}(\sin^2(\theta^{0',i'}_{0,0'}))\right]_{NR} = \frac{2}{15}(2\cos^2(\theta^{0',i'}_{0,0'}) + 1), \quad (12)$$

$$(Y_1)_{YYZZ} = \left[\tilde{Y}^{zzzz}_{YYZZ}(\cos^2(\theta^{0',i'}_{0,0'})) + \tilde{Y}^{yyzz}_{YYZZ}(\sin^2(\theta^{0',i'}_{0,0'}))\right]_R + \left[\tilde{Y}^{zzzz}_{YYZZ}(\cos^2(\theta^{0',i'}_{0,0'})) + \tilde{Y}^{yyzz}_{YYZZ}(\sin^2(\theta^{0',i'}_{0,0'}))\right]_{NR} = \frac{2}{15}(1 + \sin^2(\theta^{0',i'}_{0,0'})). \quad (13)$$

The anisotropy of pathway $II^{i}_{O,O}$ is found using Eq. (11), yielding the expected relationship for a pathway with an orientational response dependent upon a single angle. For a spectrally isolated pathway $II^{i}_{O,O}$, the 2D EV anisotropy directly reports on the angle between the excited state vibrational mode $i$ and the fundamental electronic transition, $\boldsymbol{\mu}^{0,0'}$. Similarly, pathway $II^{j}_{O,O}$ has the same form of angular dependence and anisotropy relations, as do the corresponding GSB pathways, $I^{i}_{O,O}$ and $I^{j}_{O,O}$.

The anisotropy relations described above can be used systematically on different 2D EV and 2D VE pathways with different angle dependencies to obtain further insight into the molecular frame. For example, consider the 2D EV pathways $I^{i}_{O,O}$, $II^{j}_{O,O}$, and $III^{i}_{i,O}$. The $Y_{ZZZZ}$, $Y_{YYZZ}$, and $r(\theta^{0,i}_{0,0'})$ are plotted in Fig. 4(a) for 2D EV pathway $I^{i}_{O,O}$. The parallel and perpendicular responses are equal at the magic angle, 54.7°, and the anisotropy parameter ranges from 0.4 when $\hat{\mu}^{0,i} \parallel \hat{\mu}^{0,0'}$ to −0.2 when $\hat{\mu}^{0,i} \perp \hat{\mu}^{0,0'}$. The unit vectors (i.e., $\hat{\mu}$) are specifically used in discussing the values of $r(\theta)$ to emphasize the assumptions made in the analysis and outlined above. We note that the magnitudes of the dipole moments may still distort $r(\theta)$ from this range of values as a result of non-Condon effects and Duschinsky mixing; this is thoroughly outlined in Secs. III–V of the Paper II in this series.[76] From the experimental observable, $r(\theta^{0,i}_{0,0'})$, the angle between the ground state vibrational dipole moment of oscillator $i$ ($\hat{\mu}^{0,i}$) and the fundamental electronic transition dipole moment ($\hat{\mu}^{0,0'}$) is determined. With $\theta^{0,i}_{0,0'}$ defined, the ground state vibrational transition dipole moment can be used as a molecular-frame point of reference for determining the relative orientation of other dipole moments. For example, the existence of a nonzero angle between $\hat{\mu}^{0,0'}$ and $\hat{\mu}^{0,i'}$ ($\theta^{0,i'}_{0,0'} \neq 0$) provides evidence that a vibrational coordinate dependence of the electronic transition is present in the molecular system under investigation. Since the GSB $III^{i}_{i,O}$ depends on both $\theta^{0,i}_{0,0'}$ and $\theta^{0,i'}_{0,0'}$, this pathway can be used to determine $\theta^{0,i'}_{0,0'}$. The two-angle dependent anisotropy for $III^{i}_{i,O}$ is plotted in Fig. 4(b). Using the determined value of $\theta^{0,i}_{0,0'}$ from pathway $I^{i}_{O,O}$, this two-dimensional anisotropy is reduced to only a dependence on $\theta^{0,i'}_{0,0'}$, which can then be determined from the empirical anisotropy of pathway $III^{i}_{i,O}$.

Another way of quantifying angles between various dipole moments is through the ratio of anisotropies measured for different pathways. As shown in Figs. 4(c) and (d), the anisotropy ratios between pathways that contain at least one common transition dipole moment can be used to identify the difference between the two pathways' angular dependence. The 2D EV GSB pathway $I^{i}_{O,O}$ and ESA pathway $II^{i}_{O,O}$ share the same electronic transition dipole moment, $\boldsymbol{\mu}^{0,0'}$; thus, these pathways can be used to determine the difference in the vibrational transition dipole moments involved in these transitions. Figure 4(c) plots the 2D EV anisotropy ratio ($II^{i}_{O,O}/I^{i}_{O,O}$) for various values of $\theta^{0,i}_{0,0'}$, which are determined by Fig. 4(a). Anisotropy ratios differing from 1 indicate that the vibrational motion of oscillator $i$ changes direction upon electronic excitation. The excited state angle can be read directly from the plot in Fig. 4(c). A similar relationship between pathways $I^{i}_{O,O}$ and $III^{i}_{i,O}$ exists, as implied by Fig. 4(b) and the discussion above. The common dipole moment of these two pathways is $\boldsymbol{\mu}^{0,i}$, and they differ by their electronic transitions. Recasting the anisotropy relationships

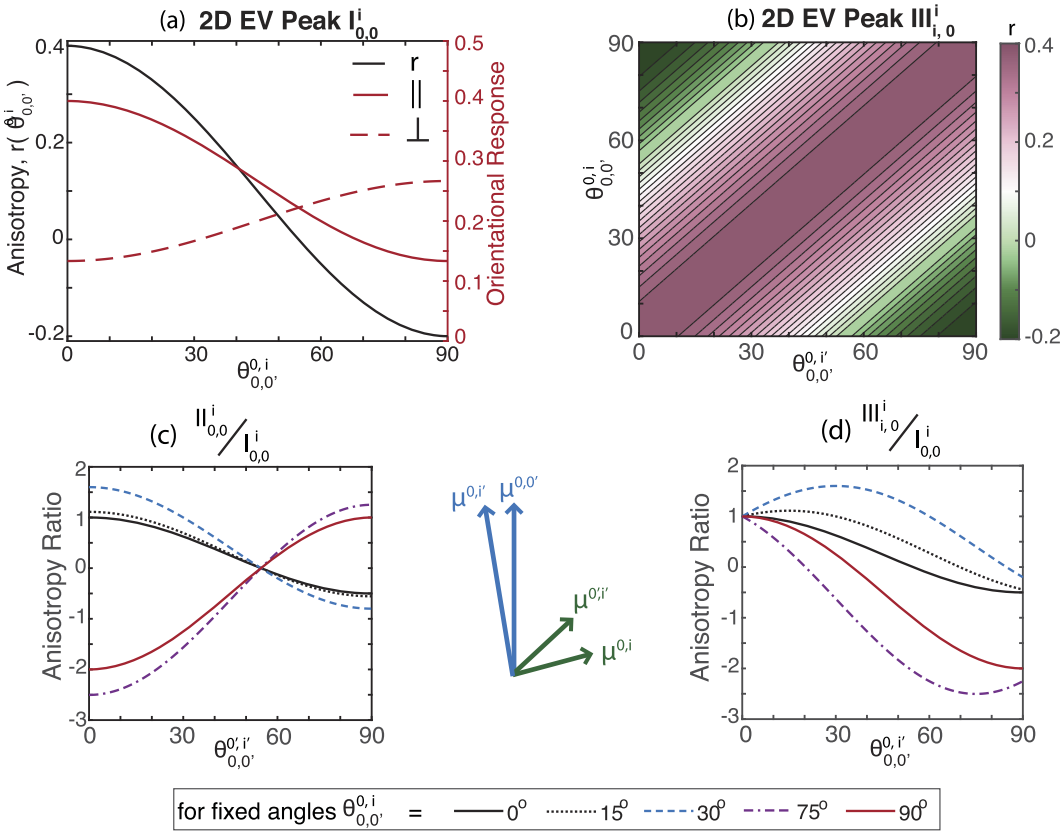


**FIG. 4**. Systematic anisotropy analysis using multiple 2D pathways. (a) The orientational response and anisotropy for 2D EV pathway $I^i_{0,0}$. (b) The anisotropy for 2D EV pathway $III^i_{i,0}$ depends on two angles: the electronic dipole moment $\hat{\mu}^{0,i'}$ with angle $\theta^{0,i'}_{0,0'}$ and the vibrational dipole moment $\hat{\mu}^{0,i}_{0,0'}$ with angle $\theta^{0,i}_{0,0'}$ (contours given with 5% intervals). The anisotropy ratios of pathways with different dipole moments are plotted in (c) and (d) to illustrate how various angles may be extracted by considering multiple pathways in the 2D EV spectrum. For a determined angle $\theta^{0,i}_{0,0'}$, the relative angles between the ground and excited state vibrational mode can be obtained [as in (c)] and the relative angles between the electronic dipole moments $\hat{\mu}^{0,0'}$ and $\hat{\mu}^{0,i'}$ can be determined [as in (d)]. Note that these figures and the discussion assume that the vibronic response is effectively unity such that the relative amplitudes are governed only by orientational response.

between these two GSB pathways as a ratio yields Fig. 4(d), where the nuclear coordinate dependence of the $\hat{\mu}^{0,i'}$ is readily identified through an anisotropy ratio differing from 1. While these examples have used specific 2D EV pathways, the analytical approach is generalizeable to any set of 2D vibronic pathways with the same relationships of angular dependence described above. This approach can also be extended to narrow down the angular dependence of pathways that depend on four angles.

Anisotropy analyses using both 2D EV and 2D VE features naturally increases the set of dipole moments that can be investigated when studying a molecular system. While the anisotropy ratios for the 2D EV pathways in Fig. 4(d) use the GSBs to explore the presence of non-Condon effects, the analogous comparison in 2D VE spectroscopy lends a different perspective on non-Condon effects through the orientational response. In particular, the 2D VE pathway $II^i_{i,i}$ uses the electronic dipole moment $\boldsymbol{\mu}^{i,i'}$, which is inaccessible to 2D EV spectroscopy. Since the 2D VE pathway $I^O_{i,O}$ accesses $\boldsymbol{\mu}^{0,0'}$, the anisotropy ratio of these two pathways is directly sensitive to how vibrational mixing in either electronic state affects the projection of the ground state vibrational coordinate onto the electronically excited state potential. In cases where spectral overlap in 2D VE features inhibits direct anisotropic analysis, the use of an analogous 2D EV GSB pathway that employs the same dipole moments can facilitate the anisotropy analysis. For example, since the 2D EV pathway $I^i_{O,O}$ and 2D VE pathway $I^O_{i,O}$ both use $\boldsymbol{\mu}^{0,0'}$ and $\boldsymbol{\mu}^{0,i}$, the anisotropy ratios of each of these pathways with the 2D VE ESA pathway $II^i_{i,i}$ contain identical information. Additionally, better $\omega_3$ spectral resolution of the 2D EV anisotropy afforded by vibrationally resonant probing should help the comparison of these two anisotropy ratios to provide a more consistent analysis of the 2D VE anisotropy ratio. That is, by finding the $\omega_3$ frequencies where these two ratios approach the same value would provide more confidence in the determination of $\theta^{i,i'}_{0,0'}$, which is only accessible through 2D VE ESA pathways. For systems in which the Franck–Condon

approximation is valid, it is expected that $\hat{\mu}^{0,0'} \cong \hat{\mu}^{i,i'}$. However, the presence of non-Condon effects and Duschinsky mixing will render $\theta_{0,i}^{0,0'}$ and $\theta_{0,i}^{i,i'}$ to have increasingly different values due to the different vibronic dipole moments on which these angles depend. This example suggests one way that an anisotropy comparison between specific pathways measured in 2D EV and 2D VE spectroscopy can be used in tandem to help quantify non-Condon effects. On a broader level, it is notable that the 2D EV and 2D VE spectroscopies can directly interrogate the $\boldsymbol{\mu}^{0,i'}$ and $\boldsymbol{\mu}^{0,j'}$ transition dipole moments in comparison to the fundamental electronic transition dipole moment $\boldsymbol{\mu}^{0,0'}$.

It is important to note that an absolute—as opposed to relative—determination of the dipole orientations can be ambiguous due to the $\pi$-periodic nature of the anisotropy relations.[42] For example, determining $\theta_{0,0'}^{0',i'} = 20^o$ using Fig. 4(c) cannot distinguish between the full range of solutions $\theta_{0,0'}^{0',i'} = 20^o \pm 180^o$. Therefore, when the anisotropy ratios equal 1 in Figs. 4(c) and 4(d), the dipole moments of interest may either be parallel or antiparallel to the shared dipoles between the two pathways being investigated. However, it is reasonable to assume that such large changes in dipole moments would not retain similar enough character to be comparable in the manner discussed here and so are outside the scope of this discussion; much smaller angles are expected in practice. Notably, the anisotropy ratios also become ill-defined and diverge asymptotically as the reference dipole moment angle approaches the magic angle where $r \to 0$.[86]

## B. Brief comparison between observables in 2D vibronic spectroscopies and other nonlinear techniques

As 2D EV and 2D VE spectroscopies are more widely applied to a variety of scientific questions, it is useful to directly discuss how some of the observables in these newer techniques compare to other ultrafast nonlinear techniques that have been used to study molecular structural dynamics.

### 1. Transient-IR (tIR) spectroscopy vs 2D EV spectroscopy

Transient-IR (tIR) spectroscopy—the one-dimensional analog to 2D EV spectroscopy—has employed polarization-selectivity in femtosecond chemical dynamics investigations to better understand excited state chemical phenomena.[87] In principle, the tIR spectrum is obtained from a corresponding 2D EV spectrum by integrating over the excitation frequency domain. As a result, any discernment of excitation-dependent features in the 2D EV spectrum is lost. Generally, the differences between the tIR signal amplitudes and the $\omega_1$-dependent 2D EV signal amplitudes shows that an inaccurate assessment of the excited state molecular structure could be obtained from the tIR signal alone. This observation was emphasized for consideration of only one vibration studied using these 2D vibronic spectroscopies,[53] but the effect clearly worsens as more degrees of freedom are at play in the system of interest, and as polarization-selectivity is deliberately employed to extract molecular-frame information. A multimode vibronic system has even more oppositely signed pathways with different orientational and vibronic responses, which are all convolved in the tIR spectrum as the $\omega_1$ dimension is integrated away. This fact is easily understood by considering the 2D EV cartoon schematic in Fig. 2. The molecular system described by this schematic spectrum is one in which all vibronic eigenstates assume the maximum degree of pathway separation through various intramolecular couplings; even in this case, there are only two spectral features that would not be convolved with at least one other pathway composed of very different molecular transitions in a tIR spectrum. The spectral intensities and the anisotropy values are affected for most 2D EV pathways, potentially making the tIR anisotropy values unreliable for extracting an accurate, quantitative picture of the molecular frame. For example, considering the anisotropy of a GSB feature in a t-IR experiment at $\omega_3 = \omega_i$ would convolute the effects of dipole moment angles $\theta_{0,0'}^{0,i}$, $\theta_{0,0'}^{0,i'}$, and $\theta_{0,0'}^{0,j}$ by integrating signals from pathways $\mathrm{I}_{0,0}^{i}$, $\mathrm{III}_{i,0}^{i}$, and $\mathrm{III}_{j,0}^{i}$. Consideration of the angular dependence for pathways with common $\omega_3$ frequencies shown in the Appendix illustrates further sources of inaccuracy possible through a polarization-selective t-IR experiment. Of course, this effect becomes more problematic for tIR spectral interpretation as electric fields with broader bandwidths are used for excitation. Conversely, narrower band excitation sources used in tIR experiments would mitigate this spectral convolution. By separating out the $\omega_1$-dependent pathways in the 2D EV experiment, the separation of spectral contributions arising from differently overlapped pathways in the $\omega_3$ domain is achieved. Inevitably, for molecular systems in which some of the vibronic eigenstates are not well separated (e.g., if $\Delta_{eg,i}$ is much smaller than the vibrational line width), even the polarization-dependent 2D EV spectrum will contain spectrally overlapping features of very different character.

### 2. Transient-2D IR (t-2D IR) spectroscopy vs 2D vibronic spectroscopies

One approach to measuring electronically excited state molecular structural dynamics is by incorporating an additional electronic excitation pulse that precedes the third-order 2D IR pulse sequence. This technique known as transient-2D IR (t-2D IR) spectroscopy has been successful, in particular, applications for studying excited state charge transfer of transition metal complexes.[88–90] The promise of t-2D IR spectroscopy lies in the measurement of excited state vibrational anharmonicities and frequency shifts through a difference measurement between 2D IR spectra of the ground and excited electronic states. However, the signal levels in t-2D IR spectroscopy are inherently much weaker due to their fifth-order dependence on the molecular response. As shown in the schematic spectra (Figs. 2 and 3), all of the same observables are accessible through 2D EV and 2D VE spectroscopies, which are third-order nonlinear techniques. From Figs. 2 and 3, we see that the pathway positions directly describe the excited state anharmonicities ($\Delta_{i'}$, $\Delta_{j'}$, $\Delta_{i'j'}$) and excited state vibrational frequency shifts ($\Delta_{eg,i}$, $\Delta_{eg,j}$). Noting that third-order nonlinear signals are stronger than fifth order signals, we expect that the above information can be more easily accessed with 2D vibronic spectroscopy as opposed to t-2D IR. It is important to note that the t-2D IR spectrum is capable of *simultaneously* measuring the vibrational anharmonicity in both the ground and the excited electronic states of a molecule. This information is not as directly discernible in 2D EV or 2D VE spectroscopy because neither of these third-order techniques directly access the two-quantum manifold of the ground electronic state. Polarization-selective 2D EV and 2D VE spectroscopies provide very direct routes to measuring Duschinsky

mixing. When excited state vibrational frequency shifting is of interest, the 2D EV experiment has a notable advantage over t-2D IR because the degree of mechanical anharmonicity does not determine the signal strength in 2D EV spectra, as it does in t-2D IR. Thus, the $\Delta_{eg,i}$ or $\Delta_{eg,j}$ parameter is more directly measured with 2D EV. In principle, 2D VE spectroscopy also measures excited state frequency shifting more directly than t-2D IR, but the inherently overlapping features in $\omega_3$ may limit the direct extraction of this information.

### C. Selective pathway enhancement through polarization schemes

The use of polarization schemes to enhance various signals compared to others is a common strategy in both 2D IR and 2D ES spectroscopies that has been treated in-depth elsewhere.[20,21,35,36,42,85,91,92] Specifically, polarization control in 2D IR has been used to enhance cross peaks and, more recently, perform bulk-forbidden, surface specific experiments.[22,38,93] Many of these studies are focused on the cross peaks where two different dipoles interact. These strategies are applicable directly to 2D EV and 2D VE spectroscopies where every transition pathway includes at least two different dipole moments.

The $\boldsymbol{Y}_{ZYYZ}$ and $\boldsymbol{Y}_{ZYZY}$ polarization configurations can be used to isolate all pathways in both 2D EV and 2D VE spectroscopies that experience a $\tau_2$ coherence. There is an inherent separation of purely vibrational and vibronic transitions between the $\boldsymbol{k}_1$ and $\boldsymbol{k}_2$ interactions relative to the $\boldsymbol{k}_3$ and $\boldsymbol{k}_4$ interactions in 2D EV and 2D VE spectroscopy. Assuming that rotational diffusion is negligible during the pulse sequence, the $\boldsymbol{k}_1$ and $\boldsymbol{k}_2$ ordering of the dipole projections into the laboratory frame (ZY vs YZ) for the $\tau_2$ population pathways is inconsequential because the same dipole is projected onto both axes. In fact, $\tau_2$-dependent dynamics of population pathways could provide some measure of rotational diffusion during the experiment if the rotational diffusion timescale is comparable to the population relaxation timescale.

On the other hand, the pathways involving four unique dipole moments possess very different orientational responses. When separate transition dipole moments are driven by $\boldsymbol{k}_1$, $\boldsymbol{k}_2$, $\boldsymbol{k}_3$, and $\boldsymbol{k}_4$ interactions, the pathway amplitudes are sensitive to which dipole is projected onto the laboratory frame Z and Y axes. As discussed above, all pathways involving four distinct transition dipole moments propagate as coherent superpositions during $\tau_2$. For example, pathways VII in 2D VE spectroscopy lie almost perfectly on top of pathways I and II. However, in the absence of Duschinsky mixing, pathways VII carry little intensity due to the inherently low Frank–Condon overlap of the vibronic transition resulting in a change of both vibrational quanta (e.g., $|g;01\rangle \rightarrow |e;1'0'\rangle$). Since pathways I and II have an identical response under the $\boldsymbol{Y}_{ZYYZ}$ and $\boldsymbol{Y}_{ZYZY}$ polarization schemes, the difference between these two spectra eliminates contributions of pathways I and II and enhances those of pathway VII.

The orientational responses for the $\boldsymbol{Y}_{ZZZZ} + 2\boldsymbol{Y}_{YYZZ}$ and the $\boldsymbol{Y}_{ZYZY} - \boldsymbol{Y}_{ZYYZ}$ polarization combinations for 2D EV and 2D VE pathways involving four different transition dipole moments are expressed in terms of $\Delta\theta_{12}$ and $\Delta\theta_{34}$, where $\Delta\theta_{12} = \theta_1 - \theta_2$ and $\Delta\theta_{34} = \theta_3 - \theta_4$ in Eq. (14). The angular dependence of these polarization schemes is shown by plotting $\boldsymbol{Y}_{ZYZY} - \boldsymbol{Y}_{ZYYZ}$ and its comparison to $\boldsymbol{Y}_{ZZZZ} + 2\boldsymbol{Y}_{YYZZ}$ in Fig. 5. The angles $\theta_1$, $\theta_2$, $\theta_3$, and $\theta_4$ are the angles between $\hat{\mu}^{0,0'}$ and the transition dipole moments accessed by the light–matter interactions of $\boldsymbol{k}_1$, $\boldsymbol{k}_2$, $\boldsymbol{k}_3$, and $\boldsymbol{k}_{sig}$, respectively. As given in Eq. (14a), the $\boldsymbol{Y}_{ZZZZ} + 2\boldsymbol{Y}_{YYZZ}$ response approaches the expected value of 1/3 as $\Delta\theta_{12}$ and $\Delta\theta_{34}$ approach 0°, becoming parallel and yielding what is known as the isotropic response. This case clearly reduces the complexity of the system such that a measurement of an angle of interest between, for example, $\boldsymbol{k}_2$ and $\boldsymbol{k}_3$ could be reliably extracted from $r(\theta)$. However, it is clear that the $\boldsymbol{Y}_{ZZZZ} + 2\boldsymbol{Y}_{YYZZ}$ response retains angular dependence for all pathways in a system with four non-parallel transition dipole moments,

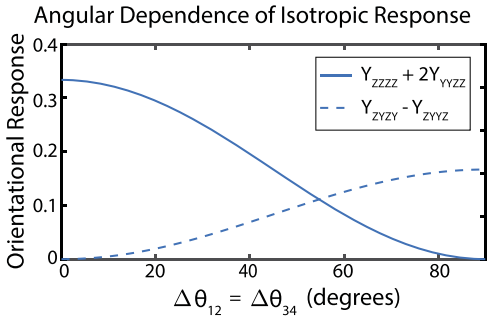


**FIG. 5**. Polarization-selective responses with ZYZY and ZYYZ polarization combinations. The orientational response is compared for a system with four non-parallel dipole moments with the polarization combinations $\boldsymbol{Y}_{ZZZZ} + 2\boldsymbol{Y}_{YYZZ}$ (solid blue) and $\boldsymbol{Y}_{ZYZY} - \boldsymbol{Y}_{ZYYZ}$ (dashed blue). The responses are plotted as a function of $\Delta\theta_{12}$, the difference between angles $\theta_1$ and $\theta_2$, and of $\Delta\theta_{3,4}$, the difference between angles $\theta_3$ and $\theta_4$. The angles $\theta_1$, $\theta_2$, $\theta_3$, and $\theta_4$ are the respective angles formed between $\hat{\mu}^{0,0'}$ and the dipole moments driven by $\boldsymbol{k}_1$, $\boldsymbol{k}_2$, $\boldsymbol{k}_3$, and $\boldsymbol{k}_{sig}$. For simplification, the orientational responses are only plotted for the condition $\Delta\theta_{12} = \Delta\theta_{34}$.

$$\boldsymbol{Y}_{ZZZZ} + 2\boldsymbol{Y}_{YYZZ} = \frac{1}{6}[\cos(\Delta\theta_{12} + \Delta\theta_{34}) + \cos(\Delta\theta_{12} - \Delta\theta_{34})], \quad (14a)$$

$$\begin{aligned}\boldsymbol{Y}_{ZYZY} - \boldsymbol{Y}_{ZYYZ} &= \frac{1}{12}[\cos(\Delta\theta_{12} + \Delta\theta_{34}) - \cos(\Delta\theta_{12} - \Delta\theta_{34})] \\ &= -\frac{1}{6}\sin(\Delta\theta_{12})\sin(\Delta\theta_{34}). \quad (14b)\end{aligned}$$

This same angular dependence can be used productively in more creative polarization combinations; an example is described in Eq. (14b). The angular dependence of the $\boldsymbol{Y}_{ZYZY} - \boldsymbol{Y}_{ZYYZ}$ polarization-dependent signal becomes zero for all pathways in which fewer than four dipole moment angles are non-zero. Observation of this particular polarization-dependent signal immediately confirms a more complicated orientational response than just a single angle dependence. The comparison of the $\boldsymbol{Y}_{ZYZY} - \boldsymbol{Y}_{ZYYZ}$ difference and the isotropic signal demonstrates the signal enhancement that is achievable. Spectral analysis taking advantage of these polarization combinations is discussed at more length in Paper II within the context of 2D vibronic spectral simulations.

The $\boldsymbol{Y}_{ZYZY} - \boldsymbol{Y}_{ZYYZ}$ polarization combination can be exploited in all regions of the 2D VE spectrum, for example, eliminating pathways III, IV, and $\tau_2$ populations in VI to isolate pathways VI with $\tau_2$ coherence or eliminating the $\tau_2$ population pathways V to amplify the multimode pathways V. In 2D EV spectroscopy, it can

be used to selectively interrogate pathways V and VI for identical reasons. In general, each $\tau_2$ coherence pathway for both spectroscopies has a partner pathway. That is, for each of these pathways there exists another $\tau_2$ coherence pathway sharing the same four dipole moments, but their temporal order of interaction is different, resulting in spectral separation of these pathways in the $(\omega_1, \omega_3)$ plane. In 2D VE spectra, pathways producing such signals contribute intensity to peaks that often overlap in $\omega_3$ (e.g., those generating R and NR $V^0_{i,j}$, see Fig. 3). The pathway pairs mentioned above acquire opposite signs in the $\boldsymbol{Y}_{ZYZY} - \boldsymbol{Y}_{ZYYZ}$ difference spectrum, resulting in more easily separated signals in the $\omega_3$ dimension.

To date, the polarization conditions of ZYZY and ZYYZ have not been realized experimentally for 2D VE or 2D EV experiments. The experimental requirement of phase-stable interferometric precision for $\boldsymbol{k}_1$ and $\boldsymbol{k}_2$ lends the implementation of these polarization schemes more amenable to 2D VE spectroscopy over 2D EV spectroscopy. Studies using 2D EV spectroscopy have been performed with pulse shapers to generate two collinear pump pulses with complete amplitude and phase shaping control.[49,51,52] As a result, $\boldsymbol{k}_1$ and $\boldsymbol{k}_2$ necessarily must have the same linear polarization.[94] While there are examples of polarization-selective 2D ES experiments with independently controlled excitation fields,[3,37] these actively phase-stabilized UV–visible interferometers have yet to be incorporated into a 2D EV experiment. However, the Mach–Zender mid-IR interferometer used to generate pulse pairs in 2D VE spectroscopy may be readily adapted to such polarization schemes.[50,57,95] The partially collinear pump–probe geometry has been used in all cases of 2D EV and 2D VE spectroscopies published to-date; this is largely for convenience because the energetic discrepancy between the electronic and vibrational resonances will result in poor spatial separation of signals in a non-collinear geometry. A notable experimental challenge will be incorporating an external local oscillator as the ZYZY and ZYYZ polarization schemes require orthogonal $\boldsymbol{E}_3$ and $\boldsymbol{E}_{sig}$ fields—precluding the direct use of the self-heterodyned detection with $\boldsymbol{E}_3$, as employed in the pump–probe geometry.

### D. $\tau_2$ dependent dynamics and anisotropies

In 2D VE spectroscopy, pathways V–VII have an $(\omega_1, \omega_3)$ coordinate mismatch between the R and NR pathway positions, complicating data interpretation. As discussed earlier, the spectrally separated R and NR pathway pairs propagate as a coherent superposition during $\tau_2$. In cases where the R and NR pathway pairs form spectrally overlapped pathways with other 2D pathways (e.g., those with $\tau_2$ populations), the $\tau_2$-dependent amplitude oscillations characteristic of these R and NR pathway pairs can be used to target these pathway or selectively remove them from interfering with the $\tau_2$ population pathways.

In Fig. 6, the lower energy $\omega_3$ manifold of a 2D VE schematic (i.e., the block of pathways V) is illustrated for two different series of $\tau_2$ delays, as the $\tau_2$-coherence pathways beat repeatedly. The first schematic [Fig. 6(a)] shows all pathways V plotted at $\tau_2 = n(\Delta\omega)^{-1}$ for any integer value of $n$, where $(\Delta\omega = |\omega_j - \omega_i|)$. The $\tau_2$-coherence R contributions of $V^0_{i,j}$ and $V^0_{j,i}$ occupy the same $(\omega_1, \omega_3)$ positions as the $\tau_2$ population pathways $V^0_{i,i}$ and $V^0_{j,j}$, whereas the NR coherence pathways of $V^0_{i,j}$ and $V^0_{j,i}$ are spectrally isolated. As a result,

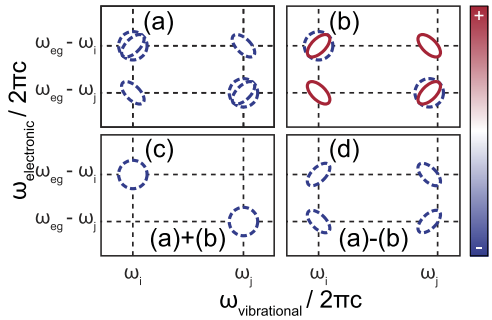


**FIG. 6. Distinguishing population and coherence pathways by $\tau_2$-dependence.** (a) 2D VE excited state absorption pathways V at $\tau_2 = n(\Delta\omega)^{-1}$ for integer values of $n$, where $\Delta\omega = |\omega_j - \omega_i|$ is the frequency difference between the two vibration. All pathways constructively interfere and contribute signals. (b) The same set of 2D VE pathways at $\tau_2 = (n + 1/2)(\Delta\omega)^{-1}$; the coherence pathways destructively interfere at these $\tau_2$ delays. (c) Coherence pathways are eliminated by summing the panels (a) and (b); the positive and negative interferences of the coherence signals at these $\tau_2$ points yield their elimination. (d) Likewise, population pathways are eliminated by the difference of the panels (a) and (b). See the 2D VE schematic in Fig. 3 for referencing pathway labels.

the R pathways skew the line shape of the $\tau_2$ population pathways. All four $\tau_2$ coherence pathways oscillate in $\tau_2$ with the same period because they all experience a coherence between the same two states ($|g;10\rangle\langle g;01|$). Theoretically, this means they all reach relative extrema simultaneously. The schematic in Fig. 6(b) at $\tau_2 = (n + 1/2)(\Delta\omega)^{-1}$ shows the impact of simply choosing a value of $\tau_2$ where the $V^0_{i,j}$ and $V^0_{j,i}$ destructively interfere to distinguish these pathways. The $\tau_2$-dependent constructive and destructive interference of the coherence pathways can be used to further isolate signals of interest. Data from the $\tau_2$ points represented in Figs. 6(a) and 6(b) can be used to eliminate the coherence pathways by their sum [Fig. 6(c)], thus enabling use of the center line slope or other analyses[25] on the population pathways $V^0_{i,i}$ and $V^0_{j,j}$. Similarly, if the coherence pathways are of greater interest, the population pathways may be eliminated by the difference of the 2D VE signals collected at $\tau_2 = n(\Delta\omega)^{-1}$ and $\tau_2 = (n + 1/2)(\Delta\omega)^{-1}$, as depicted in Fig. 6(d). In practice, this analysis would be limited by the residual dispersion of the pulses used in the experiment, yielding the best results with well characterized, fully compressed broadband pulses.

The above analysis underscores the importance of obtaining 2D VE spectra at a series of linearly spaced waiting times over which a Fourier transform is performed to resolve the third-order molecular response of the system within the parameter space accessible to the experiment. The resultant three-dimensional (3D) spectrum consists of cross peaks in the $(\omega_1, \omega_2, \omega_3)$ coordinate space. Compared to using a well-chosen $\tau_2$ delay time that enhances particular features of interest, 3D spectroscopy is effectively the frequency-domain equivalent of such spectral filtering. The $\tau_2$ population peaks will approach the DC line ($\approx 0$ cm$^{-1}$) in the 3D VE spectrum due to much slower lifetime decay by comparison to the faster oscillations characteristic of the $\tau_2$ coherent oscillations. Employing these types of strategies will allow isolation of multiple coherences in the case where more than two vibrational modes exist, including high

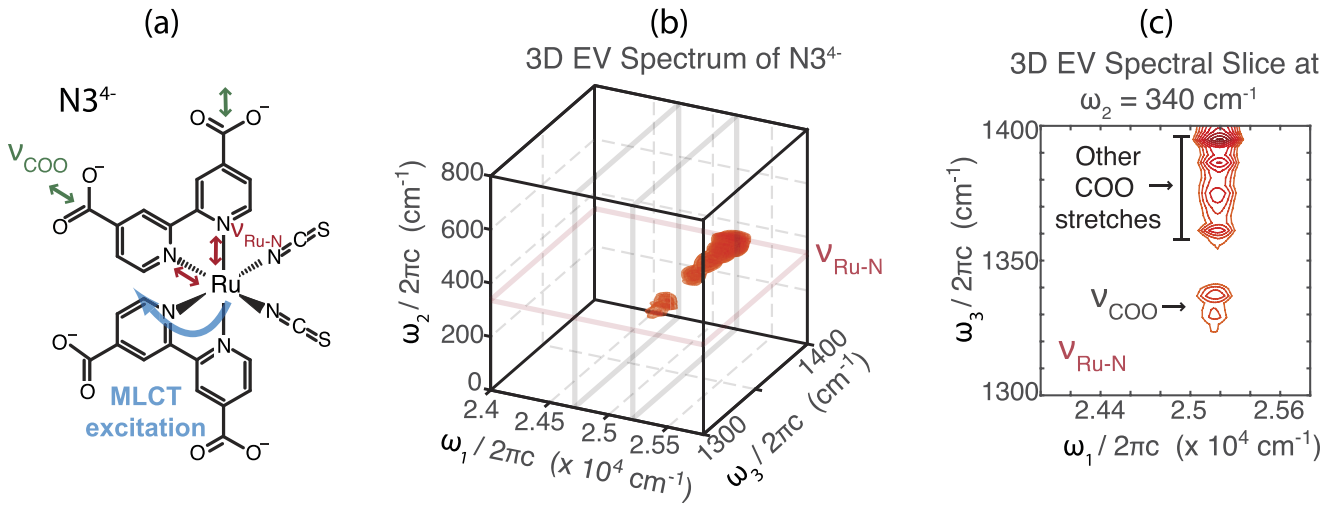


**FIG. 7**. Spectral deconvolution with $\tau_2$-dependent 2D EV amplitudes. (a) The molecular structure of [*Ru* − (*dcbpy*)$_2$(*NCS*)$_2$] (dcbpy = 4,4′-dicarboxy-2,2′-bipyridine), also known as $N3^{4-}$, with the relevant degrees of freedom highlighted: metal-to-ligand-charge-transfer (MLCT) excitation (light blue), a carboxylate symmetric stretch $\nu_{COO}$ (green), and a low frequency vibration involved in the excited state coherence evolution, $\nu_{Ru-N}$. (b) The early time ($0 < \tau_2 < 600$ fs) 3D EV spectrum of $N3^{4-}$ showing the vibronic couplings between all three degrees of freedom highlighted in (a). (c) A spectral slice of the 3D EV spectrum at the $\nu_{Ru-N}$ vibrational frequency (340 cm$^{-1}$) to demonstrate the deconvolution of the other excited state carboxylate symmetric stretches in the 1350 cm$^{-1}$ < $\omega_3$ < 1400 cm$^{-1}$ region.

frequency vibrations, low frequency vibrations, and even multiple electronic states.

The three-dimensional approach has recently proven successful in EV spectroscopy with the report of a 3D EV spectrum in the aqueous deprotonated ruthenium-centered solar cell dye molecule, $N3^{4-}$.[55] The $\tau_2$-dependence of a prominent and spectrally isolated charge accepting carboxylate symmetric stretch ($\nu_{COO}$) that vibronically couples with specific metal-to-ligand-charge-transfer excited states was used to follow the excited state evolution of vibronic coherences in $N3^{4-}$. The spectral isolation of this particular $\nu_{COO}$ reporter vibration enabled the success of this 3D EV experiment. However, calculations performed in the earlier polarization-selective 2D EV studies on $N3^{4-}$ indicate that there are actually many near-degenerate carboxylate symmetric stretches that split in the excited triplet states such that the $\nu_{COO}$ becomes spectrally isolated while the other carboxylate modes remain spectrally overlapped with their corresponding GSB features.[54] Since the vibronic coherences evolve in the excited state in $N3^{4-}$, these ESA features should have a different $\tau_2$-dependence than the corresponding GSBs and, thus, be separable in the 3D spectrum. Figure 7 shows the 3D EV spectrum of $N3^{4-}$ and a spectral slice at $\omega_2 = 340$ cm$^{-1}$, referred to as $\nu_{Ru-N}$ corresponding to a low frequency vibration involving the Ru–N stretch of the dcbpy ligands (highlighted in red). The fact that the $\nu_{Ru-N}$ is active during the vibronic coherence evolution through couplings with eigenstates of $\nu_{COO}$ character accounts for the observed $\tau_2$-dependence during the first ≈600 femtoseconds of relaxation. Moreover, this is used to deconvolve the spectrally overlapped carboxylate symmetric stretches, which is represented by the peaks in the spectral slice in the 1350 < $\omega_3$ < 1400 cm$^{-1}$ region. This is one example of how specific $\tau_2$-dependencies can be exploited to simplify the interpretation of complex 2D spectra.

## VII. CONCLUSIONS

A multimode vibronic system has been generally described in this study with emphasis on the orientational response. Various ways in which the orientational responses can be targeted to ascertain deeper insight into a multi-vibration, vibronically coupled molecular system using polarization-selective 2D EV and 2D VE spectroscopies have been thoroughly treated. This discussion may serve as a field guide to other groups interested in using 2D EV and/or 2D VE spectroscopies to directly measure vibronic dynamics in molecules. In comparison to other ultrafast nonlinear spectroscopies currently available, polarization-selective 2D EV and 2D VE spectroscopies provide unique opportunities to measure and characterize vibronic couplings, non-Condon effects, Duschinsky mixing, and electronic delocalization. Due to the complementary nature of these two techniques, an in-tandem approach to studying the vibronic couplings of molecules should give direct access to the molecular-level vibronic dynamics of interest during many photochemical phenomena, such as excited state charge transfer and excited state proton transfer. This work builds upon an expanding foundation for 2D EV and 2D VE techniques to be applied to an increasingly diverse set of scientific investigations. Future studies of vibronic Hamiltonians with multiple electronic excited states and multiple vibrations will also prove useful for interpreting experimental spectra. In Paper II of this series, the material Hamiltonian representing the system discussed here is fully described. The experimental methods and observables detailed in this paper are some of the means by which the molecular machinery described in Paper II can be accessed directly. Taken together, the work in this series of papers provides a road map for obtaining a detailed view of vibronic dynamics at the molecular level.

## SUPPLEMENTARY MATERIAL

See the supplementary material for energy gap correlation functions, dephasing functions, a complete listing of the orientational response functions, and a discussion of the rephasing and non-rephasing pathway positions for 2D vibronic spectroscopy.

## ACKNOWLEDGMENTS

The development of 2D VE spectroscopy was supported by the U.S. Department of Energy, Office of Science, Office of Basic Energy Sciences under Award No. DE-SC0019277. The development of 2D EV spectroscopy was supported by the National Science Foundation

**TABLE I**. 2D EV GSB pathways: dephasing functions (R):$R_3$, (NR):$R_4$.

| | | | Vibronic states | | | | Angles | | | | | |
|---|---|---|---|---|---|---|---|---|---|---|---|---|
| Pathway symbol | Type | Function | $\|a\rangle$ | $\|b\rangle$ | $\|c\rangle$ | $\|d\rangle$ | $\theta_1$ | $\theta_2$ | $\theta_3$ | $\theta_4$ | $\omega_1 - \omega_{eg}$ | $\omega_3$ |
| $I^i_{0,0}$ | R + NR | $F_3 + F_4$ | $\|g;0,0\rangle$ | $\|g;1,0\rangle$ | $\|g;0,0\rangle$ | $\|e;0',0'\rangle$ | (0,i) | ⋯ | ⋯ | ⋯ | 0 | $\omega_i$ |
| $I^j_{0,0}$ | R + NR | $F_3 + F_4$ | $\|g;0,0\rangle$ | $\|g;0,1\rangle$ | $\|g;0,0\rangle$ | $\|e;0',0'\rangle$ | (0,j) | ⋯ | ⋯ | ⋯ | 0 | $\omega_j$ |
| $III^i_{i,0}$ | R + NR | $F_3 + F_4$ | $\|g;0,0\rangle$ | $\|g;1,0\rangle$ | $\|g;0,0\rangle$ | $\|e;1',0'\rangle$ | (0,i′) | (0,i) | ⋯ | ⋯ | $\omega_{i'}$ | $\omega_i$ |
| $III^j_{i,0}$ | R + NR | $F_3 + F_4$ | $\|g;0,0\rangle$ | $\|g;0,1\rangle$ | $\|g;0,0\rangle$ | $\|e;1',0'\rangle$ | (0,i′) | (0,j) | ⋯ | ⋯ | $\omega_{i'}$ | $\omega_j$ |
| $III^i_{j,0}$ | R + NR | $F_3 + F_4$ | $\|g;0,0\rangle$ | $\|g;1,0\rangle$ | $\|g;0,0\rangle$ | $\|e;0',1'\rangle$ | (0,j′) | (0,i) | ⋯ | ⋯ | $\omega_{j'}$ | $\omega_i$ |
| $III^j_{j,0}$ | R + NR | $F_3 + F_4$ | $\|g;0,0\rangle$ | $\|g;0,1\rangle$ | $\|g;0,0\rangle$ | $\|e;0',1'\rangle$ | (0,j′) | (0,j) | ⋯ | ⋯ | $\omega_{j'}$ | $\omega_j$ |

**TABLE II**. 2D EV ESE pathways: dephasing functions (R):$R_2$, (NR):$R_1$.

| | | | Vibronic states | | | | Angles | | | | | |
|---|---|---|---|---|---|---|---|---|---|---|---|---|
| Pathway symbol | Type | Function | $\|a\rangle$ | $\|b\rangle$ | $\|c\rangle$ | $\|d\rangle$ | $\theta_1$ | $\theta_2$ | $\theta_3$ | $\theta_4$ | $\omega_1 - \omega_{eg}$ | $\omega_3$ |
| $V^0_{i,i}$ | R + NR | $F_1 + F_2$ | $\|g;0,0\rangle$ | $\|e;1',0'\rangle$ | $\|e;0',0'\rangle$ | $\|e;1',0'\rangle$ | (0,i′) | (0′,i′) | ⋯ | ⋯ | $\omega_{i'}$ | $\omega_{i'}$ |
| $V^0_{i,j}$ | R | $F_2$ | $\|g;0,0\rangle$ | $\|e;0',1'\rangle$ | $\|e;0',0'\rangle$ | $\|e;1',0'\rangle$ | (0,i′) | (0,j′) | (0′,j′) | (0′,i′) | $\omega_{i'}$ | $\omega_{i'}$ |
| $V^0_{i,j}$ | NR | $F_1$ | $\|g;0,0\rangle$ | $\|e;0',1'\rangle$ | $\|e;0',0'\rangle$ | $\|e;1',0'\rangle$ | (0,i′) | (0,j′) | (0′,i′) | (0′,j′) | $\omega_{i'}$ | $\omega_{j'}$ |
| $V^0_{j,i}$ | R | $F_2$ | $\|g;0,0\rangle$ | $\|e;1',0'\rangle$ | $\|e;0',0'\rangle$ | $\|e;0',1'\rangle$ | (0,j′) | (0,i′) | (0′,i′) | (0′,j′) | $\omega_{j'}$ | $\omega_{j'}$ |
| $V^0_{j,i}$ | NR | $F_1$ | $\|g;0,0\rangle$ | $\|e;1',0'\rangle$ | $\|e;0',0'\rangle$ | $\|e;0',1'\rangle$ | (0,j′) | (0,i′) | (0′,j′) | (0′,i′) | $\omega_{j'}$ | $\omega_{i'}$ |
| $V^0_{j,j}$ | R + NR | $F_1 + F_2$ | $\|g;0,0\rangle$ | $\|e;0',1'\rangle$ | $\|e;0',0'\rangle$ | $\|e;0',1'\rangle$ | (0,j′) | (0′,j′) | ⋯ | ⋯ | $\omega_{j'}$ | $\omega_{j'}$ |

**TABLE III**. 2D EV ESA pathways: dephasing functions (R):$R_1^*$, (NR):$R_2^*$.

| | | | Vibronic states | | | | Angles | | | | | |
|---|---|---|---|---|---|---|---|---|---|---|---|---|
| Pathway symbol | Type | Function | $\|a\rangle$ | $\|b\rangle$ | $\|c\rangle$ | $\|d\rangle$ | $\theta_1$ | $\theta_2$ | $\theta_3$ | $\theta_4$ | $\omega_1 - \omega_{eg}$ | $\omega_3$ |
| $II^i_{0,0}$ | R + NR | $F_1 + F_2$ | $\|g;0,0\rangle$ | $\|e;0',0'\rangle$ | $\|e;1',0'\rangle$ | $\|e;0',0'\rangle$ | (0′,i′) | ⋯ | ⋯ | ⋯ | 0 | $\omega_{i'}$ |
| $II^j_{0,0}$ | R + NR | $F_1 + F_2$ | $\|g;0,0\rangle$ | $\|e;0',0'\rangle$ | $\|e;0',1'\rangle$ | $\|e;0',0'\rangle$ | (0′,j′) | ⋯ | ⋯ | ⋯ | 0 | $\omega_{j'}$ |
| $IV^{2i}_{i,i}$ | R + NR | $F_1 + F_2$ | $\|g;0,0\rangle$ | $\|e;1',0'\rangle$ | $\|e;2',0'\rangle$ | $\|e;1',0'\rangle$ | (0,i′) | (i′,2i′) | ⋯ | ⋯ | $\omega_{i'}$ | $\omega_{i'} - \Delta_{i'}$ |
| $IV^{2j}_{j,j}$ | R + NR | $F_1 + F_2$ | $\|g;0,0\rangle$ | $\|e;0',1'\rangle$ | $\|e;0',2'\rangle$ | $\|e;0',1'\rangle$ | (0,j′) | (j′,2j′) | ⋯ | ⋯ | $\omega_{j'}$ | $\omega_{j'} - \Delta_{j'}$ |
| $VI^{ij}_{i,i}$ | R + NR | $F_1 + F_2$ | $\|g;0,0\rangle$ | $\|e;1',0'\rangle$ | $\|e;1',1'\rangle$ | $\|e;1',0'\rangle$ | (0,i′) | (i′,i′j′) | ⋯ | ⋯ | $\omega_{i'}$ | $\omega_{j'} - \Delta_{i'j'}$ |
| $VI^{ij}_{i,j}$ | R | $F_1$ | $\|g;0,0\rangle$ | $\|e;0',1'\rangle$ | $\|e;1',1'\rangle$ | $\|e;1',0'\rangle$ | (0,i′) | (0,j′) | (j′,i′j′) | (i′,i′j′) | $\omega_{i'}$ | $\omega_{j'} - \Delta_{i'j'}$ |
| $VI^{ij}_{i,j}$ | NR | $F_2$ | $\|g;0,0\rangle$ | $\|e;0',1'\rangle$ | $\|e;1',1'\rangle$ | $\|e;1',0'\rangle$ | (0,i′) | (0,j′) | (i′,i′j′) | (j′,i′j′) | $\omega_{i'}$ | $\omega_{i'} - \Delta_{i'j'}$ |
| $VI^{ij}_{j,i}$ | R | $F_1$ | $\|g;0,0\rangle$ | $\|e;1',0'\rangle$ | $\|e;1',1'\rangle$ | $\|e;0',1'\rangle$ | (0,j′) | (0,i′) | (i′,i′j′) | (j′,i′j′) | $\omega_{j'}$ | $\omega_{i'} - \Delta_{i'j'}$ |
| $VI^{ij}_{j,i}$ | NR | $F_2$ | $\|g;0,0\rangle$ | $\|e;1',0'\rangle$ | $\|e;1',1'\rangle$ | $\|e;0',1'\rangle$ | (0,j′) | (0,i′) | (j′,i′j′) | (i′,i′j′) | $\omega_{j'}$ | $\omega_{j'} - \Delta_{i'j'}$ |
| $VI^{ij}_{j,j}$ | R + NR | $F_1 + F_2$ | $\|g;0,0\rangle$ | $\|e;0',1'\rangle$ | $\|e;1',1'\rangle$ | $\|e;0',1'\rangle$ | (0,j′) | (j′,i′j′) | ⋯ | ⋯ | $\omega_{j'}$ | $\omega_{i'} - \Delta_{i'j'}$ |

**TABLE IV**. 2D VE GSB pathways: dephasing functions (R):$R_3$, (NR):$R_4$.

| | | | Vibronic states | | | | Angles | | | | | |
|---|---|---|---|---|---|---|---|---|---|---|---|---|
| Pathway symbol | Type | Function | $\|a\rangle$ | $\|b\rangle$ | $\|c\rangle$ | $\|d\rangle$ | $\theta_1$ | $\theta_2$ | $\theta_3$ | $\theta_4$ | $\omega_1$ | $\omega_3 - \omega_{eg}$ |
| $I^i_{i,i}$ | R + NR | $F_3 + F_4$ | $\|g;0,0\rangle$ | $\|e;0',0'\rangle$ | $\|g;0,0\rangle$ | $\|g;1,0\rangle$ | (0,i) | ⋯ | ⋯ | ⋯ | $\omega_i$ | 0 |
| $I^j_{j,j}$ | R + NR | $F_3 + F_4$ | $\|g;0,0\rangle$ | $\|e;0',0'\rangle$ | $\|g;0,0\rangle$ | $\|g;0,1\rangle$ | (0,j) | ⋯ | ⋯ | ⋯ | $\omega_j$ | 0 |
| $III^i_{i,0}$ | R + NR | $F_3 + F_4$ | $\|g;0,0\rangle$ | $\|e;1',0'\rangle$ | $\|g;0,0\rangle$ | $\|g;1,0\rangle$ | (0,i) | (0,i′) | ⋯ | ⋯ | $\omega_i$ | $\omega_{i'}$ |
| $III^j_{i,0}$ | R + NR | $F_3 + F_4$ | $\|g;0,0\rangle$ | $\|e;0',1'\rangle$ | $\|g;0,0\rangle$ | $\|g;1,0\rangle$ | (0,i) | (0,j′) | ⋯ | ⋯ | $\omega_i$ | $\omega_{j'}$ |
| $III^i_{j,0}$ | R + NR | $F_3 + F_4$ | $\|g;0,0\rangle$ | $\|e;1',0'\rangle$ | $\|g;0,0\rangle$ | $\|g;0,1\rangle$ | (0,j) | (0,i′) | ⋯ | ⋯ | $\omega_j$ | $\omega_{i'}$ |
| $III^j_{j,0}$ | R + NR | $F_3 + F_4$ | $\|g;0,0\rangle$ | $\|e;0',1'\rangle$ | $\|g;0,0\rangle$ | $\|g;0,1\rangle$ | (0,j) | (0,j′) | ⋯ | ⋯ | $\omega_j$ | $\omega_{j'}$ |

**TABLE V**. 2D VE ESA pathways: dephasing functions (R):$R_1^*$ (NR):$R_2^*$.

| | | | Vibronic states | | | | Angles | | | | | |
|---|---|---|---|---|---|---|---|---|---|---|---|---|
| Pathway symbol | Type | Function | $\|a\rangle$ | $\|b\rangle$ | $\|c\rangle$ | $\|d\rangle$ | $\theta_1$ | $\theta_2$ | $\theta_3$ | $\theta_4$ | $\omega_1$ | $\omega_3 - \omega_{eg}$ |
| $II^i_{i,i}$ | R + NR | $F_1 + F_2$ | $\|g;0,0\rangle$ | $\|g;1,0\rangle$ | $\|e;1',0'\rangle$ | $\|g;1,0\rangle$ | (0,i) | (i,i′) | ⋯ | ⋯ | $\omega_i$ | $\Delta_{eg,i}$ |
| $II^j_{j,j}$ | R + NR | $F_1 + F_2$ | $\|g;0,0\rangle$ | $\|g;0,1\rangle$ | $\|e;0',1'\rangle$ | $\|g;0,1\rangle$ | (0,j) | (0,j′) | ⋯ | ⋯ | $\omega_j$ | $\Delta_{eg,j}$ |
| $IV^{2i}_{i,i}$ | R + NR | $F_1 + F_2$ | $\|g;0,0\rangle$ | $\|g;1,0\rangle$ | $\|e;2',0'\rangle$ | $\|g;1,0\rangle$ | (0,i) | (i,2i′) | ⋯ | ⋯ | $\omega_i$ | $\omega_{i'} + \Delta_{eg,i} - \Delta_i$ |
| $IV^{2j}_{j,j}$ | R + NR | $F_1 + F_2$ | $\|g;0,0\rangle$ | $\|g;0,1\rangle$ | $\|e;0',2'\rangle$ | $\|g;0,1\rangle$ | (0,j) | (j,2j′) | ⋯ | ⋯ | $\omega_j$ | $\omega_{j'} + \Delta_{eg,j} - \Delta_j$ |
| $V^0_{i,i}$ | R + NR | $F_1 + F_2$ | $\|g;0,0\rangle$ | $\|g;1,0\rangle$ | $\|e;0',0'\rangle$ | $\|g;1,0\rangle$ | (0,i) | (i,0′) | ⋯ | ⋯ | $\omega_i$ | $-\omega_i$ |
| $V^0_{i,j}$ | R | $F_1$ | $\|g;0,0\rangle$ | $\|g;0,1\rangle$ | $\|e;0',0'\rangle$ | $\|g;1,0\rangle$ | (0,i) | (0,j) | (j,0′) | (i,0′) | $\omega_i$ | $-\omega_i$ |
| $V^0_{i,j}$ | NR | $F_2$ | $\|g;0,0\rangle$ | $\|g;0,1\rangle$ | $\|e;0',0'\rangle$ | $\|g;1,0\rangle$ | (0,i) | (0,j) | (i,0′) | (j,0′) | $\omega_i$ | $-\omega_j$ |
| $V^0_{j,i}$ | R | $F_1$ | $\|g;0,0\rangle$ | $\|g;1,0\rangle$ | $\|e;0',0'\rangle$ | $\|g;0,1\rangle$ | (0,j) | (0,i) | (i,0′) | (j,0′) | $\omega_j$ | $-\omega_j$ |
| $V^0_{j,i}$ | NR | $F_2$ | $\|g;0,0\rangle$ | $\|g;1,0\rangle$ | $\|e;0',0'\rangle$ | $\|g;0,1\rangle$ | (0,j) | (0,i) | (j,0′) | (i,0′) | $\omega_j$ | $-\omega_i$ |
| $V^0_{j,j}$ | R + NR | $F_1 + F_2$ | $\|g;0,0\rangle$ | $\|g;0,1\rangle$ | $\|e;0',0'\rangle$ | $\|g;0,1\rangle$ | (0,j) | (j,0′) | ⋯ | ⋯ | $\omega_j$ | $-\omega_j$ |
| $VI^{ij}_{i,i}$ | R + NR | $F_1 + F_2$ | $\|g;0,0\rangle$ | $\|g;1,0\rangle$ | $\|e;1',1'\rangle$ | $\|g;1,0\rangle$ | (0,i) | (i,i′j′) | ⋯ | ⋯ | $\omega_i$ | $\omega_{j'} + \Delta_{eg,i} - \Delta_{i'j'}$ |
| $VI^{ij}_{i,j}$ | R | $F_1$ | $\|g;0,0\rangle$ | $\|g;0,1\rangle$ | $\|e;1',1'\rangle$ | $\|g;1,0\rangle$ | (0,i) | (0,j) | (j,i′j′) | (i,i′j′) | $\omega_i$ | $\omega_{j'} + \Delta_{eg,i} - \Delta_{i'j'}$ |
| $VI^{ij}_{i,j}$ | NR | $F_2$ | $\|g;0,0\rangle$ | $\|g;0,1\rangle$ | $\|e;1',1'\rangle$ | $\|g;1,0\rangle$ | (0,i) | (0,j) | (i,i′j′) | (j,i′j′) | $\omega_i$ | $\omega_{i'} + \Delta_{eg,j} - \Delta_{i'j'}$ |
| $VI^{ij}_{j,i}$ | R | $F_1$ | $\|g;0,0\rangle$ | $\|g;1,0\rangle$ | $\|e;1',1'\rangle$ | $\|g;0,1\rangle$ | (0,j) | (0,i) | (i,i′j′) | (j,i′j′) | $\omega_j$ | $\omega_{i'} + \Delta_{eg,j} - \Delta_{i'j'}$ |
| $VI^{ij}_{j,i}$ | NR | $F_2$ | $\|g;0,0\rangle$ | $\|g;1,0\rangle$ | $\|e;1',1'\rangle$ | $\|g;0,1\rangle$ | (0,j) | (0,i) | (j,i′j′) | (i,i′j′) | $\omega_j$ | $\omega_{j'} + \Delta_{eg,i} - \Delta_{i'j'}$ |
| $VI^{ij}_{j,j}$ | R + NR | $F_1 + F_2$ | $\|g;0,0\rangle$ | $\|g;0,1\rangle$ | $\|e;1',1'\rangle$ | $\|g;0,1\rangle$ | (0,j) | (j,i′j′) | ⋯ | ⋯ | $\omega_j$ | $\omega_{i'} + \Delta_{eg,j} - \Delta_{i'j'}$ |
| $VII^i_{j,j}$ | R + NR | $F_1 + F_2$ | $\|g;0,0\rangle$ | $\|g;0,1\rangle$ | $\|e;1',0'\rangle$ | $\|g;0,1\rangle$ | (0,j) | (j,i′) | ⋯ | ⋯ | $\omega_j$ | $\omega_i - \omega_j + \Delta_{eg,i}$ |
| $VII^i_{i,j}$ | R | $F_1$ | $\|g;0,0\rangle$ | $\|g;0,1\rangle$ | $\|e;1',0'\rangle$ | $\|g;1,0\rangle$ | (0,i) | (0,j) | (j,i′) | (i,i′) | $\omega_i$ | $\Delta_{eg,i}$ |
| $VII^i_{i,j}$ | NR | $F_2$ | $\|g;0,0\rangle$ | $\|g;0,1\rangle$ | $\|e;1',0'\rangle$ | $\|g;1,0\rangle$ | (0,i) | (0,j) | (i,i′) | (j,i′) | $\omega_i$ | $\omega_i - \omega_j + \Delta_{eg,i}$ |
| $VII^i_{j,i}$ | R | $F_1$ | $\|g;0,0\rangle$ | $\|g;1,0\rangle$ | $\|e;1',0'\rangle$ | $\|g;0,1\rangle$ | (0,j) | (0,i) | (i,i′) | (j,i′) | $\omega_j$ | $\omega_i - \omega_j + \Delta_{eg,i}$ |
| $VII^i_{j,i}$ | NR | $F_2$ | $\|g;0,0\rangle$ | $\|g;1,0\rangle$ | $\|e;1',0'\rangle$ | $\|g;0,1\rangle$ | (0,j) | (0,i) | (j,i′) | (i,i′) | $\omega_j$ | $\Delta_{eg,i}$ |
| $VII^j_{i,i}$ | R + NR | $F_1 + F_2$ | $\|g;0,0\rangle$ | $\|g;1,0\rangle$ | $\|e;0',1'\rangle$ | $\|g;1,0\rangle$ | (0,i) | (i,j′) | ⋯ | ⋯ | $\omega_i$ | $\omega_j - \omega_i + \Delta_{eg,j}$ |
| $VII^j_{i,j}$ | R | $F_1$ | $\|g;0,0\rangle$ | $\|g;0,1\rangle$ | $\|e;0',1'\rangle$ | $\|g;1,0\rangle$ | (0,i) | (0,j) | (j,j′) | (i,j′) | $\omega_i$ | $\omega_j - \omega_i + \Delta_{eg,j}$ |
| $VII^j_{i,j}$ | NR | $F_2$ | $\|g;0,0\rangle$ | $\|g;0,1\rangle$ | $\|e;0',1'\rangle$ | $\|g;1,0\rangle$ | (0,i) | (0,j) | (i,j′) | (j,j′) | $\omega_i$ | $\Delta_{eg,j}$ |
| $VII^j_{j,i}$ | R | $F_1$ | $\|g;0,0\rangle$ | $\|g;1,0\rangle$ | $\|e;0',1'\rangle$ | $\|g;0,1\rangle$ | (0,j) | (0,i) | (i,j′) | (j,j′) | $\omega_j$ | $\Delta_{eg,j}$ |
| $VII^j_{j,i}$ | NR | $F_2$ | $\|g;0,0\rangle$ | $\|g;1,0\rangle$ | $\|e;0',1'\rangle$ | $\|g;0,1\rangle$ | (0,j) | (0,i) | (j,j′) | (i,j′) | $\omega_j$ | $\omega_j - \omega_i + \Delta_{eg,j}$ |

(Grant No. CHE 1856413). J.D.G. and R.B.W. acknowledge support from the NSF Graduate Research Fellowship Program under Grant No. DGE-1762114. J.D.G. acknowledges current support from the Arnold and Mabel Beckman Foundation.

## APPENDIX: PATHWAY LABELS AND ANGLE DEPENDENCE

In all cases, the $\theta_{a,b}^{c,d}$ angles are such that $a = 0$ and $b = 0'$ because they are all defined with respect to the $\boldsymbol{\mu}^{0,0'}$ dipole moment. Therefore, the subscript $(0,0')$ is omitted and only superscripts (c, d) are given for the dipole moment forming the angle with $\boldsymbol{\mu}^{0,0'}$.

### 1. 2D Electronic–Vibrational pathways

The angular dependence for 2D EV pathways is given in Tables I–III.

### 2. 2D Vibrational–Electronic pathways

The angular dependence for 2D VE pathways is given in Tables IV and V.

## DATA AVAILABILITY

The data that support the findings of this study are available from the corresponding author upon reasonable request.

## REFERENCES

[1]W. P. Aue, E. Bartholdi, and R. R. Ernst, "Two-dimensional spectroscopy. Application to nuclear magnetic resonance," J. Chem. Phys. **64**, 2229–2246 (1976).
[2]S. Mukamel, D. Abramavicius, L. Yang, W. Zhuang, I. V. Schweigert, and D. V. Voronine, "Coherent multidimensional optical probes for electron correlations and exciton dynamics: From NMR to x-rays," Acc. Chem. Res. **42**, 553–562 (2009).
[3]N. S. Ginsberg, J. A. Davis, M. Ballottari, Y.-C. Cheng, R. Bassi, and G. R. Fleming, "Solving structure in the CP29 light harvesting complex with polarization-phased 2D electronic spectroscopy," Proc. Natl. Acad. Sci. U. S. A. **108**, 3848–3853 (2011).
[4]V. R. Policht, A. Niedringhaus, and J. P. Ogilvie, "Characterization of vibrational coherence in monomeric bacteriochlorophyll a by two-dimensional electronic spectroscopy," J. Phys. Chem. Lett. **9**, 6631–6637 (2018).
[5]T. Brixner, J. Stenger, H. M. Vaswani, M. Cho, R. E. Blankenship, and G. R. Fleming, "Two-dimensional spectroscopy of electronic couplings in photosynthesis," Nature **434**, 625–628 (2005).
[6]G. S. Schlau-Cohen, A. Ishizaki, T. R. Calhoun, N. S. Ginsberg, M. Ballottari, R. Bassi, and G. R. Fleming, "Elucidation of the timescales and origins of quantum electronic coherence in LHCII," Nat. Chem. **4**, 389–395 (2012).
[7]G. S. Engel, T. R. Calhoun, E. L. Read, T.-K. Ahn, T. Mančal, Y.-C. Cheng, R. E. Blankenship, and G. R. Fleming, "Evidence for wavelike energy transfer through quantum coherence in photosynthetic systems," Nat. Lett. **446**, 782–786 (2007).
[8]E. Meneghin, A. Volpato, L. Cupellini, L. Bolzonello, S. Jurinovich, V. Mascoli, D. Carbonera, B. Mennucci, and E. Collini, "Coherence in carotenoid-to-chlorophyll energy transfer," Nat. Commun. **9**, 3160 (2018).
[9]O. Bixner, V. Lukeš, T. Mančal, J. Hauer, F. Milota, M. Fischer, I. Pugliesi, M. Bradler, W. Schmid, E. Riedle, H. F. Kauffmann, and N. Christensson, "Ultrafast photo-induced charge transfer unveiled by two-dimensional electronic spectroscopy," J. Chem. Phys. **136**, 204503 (2012).
[10]D. B. Turner, K. W. Stone, K. Gundogdu, and K. A. Nelson, "Three-dimensional electronic spectroscopy of excitons in GaAs quantum wells," J. Chem. Phys. **131**, 144510 (2009).
[11]A. Jha, H.-G. Duan, V. Tiwari, P. K. Nayak, H. J. Snaith, M. Thorwart, and R. J. D. Miller, "Direct observation of ultrafast exciton dissociation in lead iodide perovskite by 2D electronic spectroscopy," ACS Photonics **5**, 852–860 (2018).
[12]D. B. Turner, P. Wen, D. H. Arias, and K. A. Nelson, "Coherent two-exciton dynamics measured using two-quantum rephasing two-dimensional electronic spectroscopy," Phys. Rev. B **84**, 165321 (2011).
[13]A. Halpin, P. J. M. Johnson, R. Tempelaar, R. S. Murphy, J. Knoester, T. L. C. Jansen, and R. J. D. Miller, "Two-dimensional spectroscopy of a molecular dimer unveils the effects of vibronic coupling on exciton coherences," Nat. Chem. **6**, 196–201 (2014).
[14]D. Abramavicius, B. Palmieri, D. V. Voronine, F. Šanda, and S. Mukamel, "Coherent multidimensional optical spectroscopy of excitons in molecular aggregates; quasiparticle versus supermolecule perspectives," Chem. Rev. **109**, 2350–2408 (2009).
[15]F. Milota, V. I. Prokhorenko, T. Mancal, H. Von Berlepsch, O. Bixner, H. F. Kauffmann, and J. Hauer, "Vibronic and vibrational coherences in two-dimensional electronic spectra of supramolecular J-aggregates," J. Phys. Chem. A **117**, 6007–6014 (2013).
[16]Y. S. Kim and R. M. Hochstrasser, "Chemical exchange 2D IR of hydrogen-bond making and breaking," Proc. Natl. Acad. Sci. U. S. A. **102**, 11185–11190 (2005).
[17]J. Kübel, G. Lee, S. A. Ooi, S. Westenhoff, H. Han, M. Cho, and M. Maj, "Ultrafast chemical exchange dynamics of hydrogen bonds observed via isonitrile infrared sensors: Implications for biomolecular studies," J. Phys. Chem. Lett. **10**, 7878–7883 (2019).
[18]K. Kwak, J. Zheng, H. Cang, and M. D. Fayer, "Ultrafast two-dimensional infrared vibrational echo chemical exchange experiments and theory," J. Phys. Chem. B **110**, 19998–20013 (2006).
[19]K. M. Slenkamp, M. S. Lynch, B. E. Van Kuiken, J. F. Brookes, C. C. Bannan, S. L. Daifuku, and M. Khalil, "Investigating vibrational anharmonic couplings in cyanide-bridged transition metal mixed valence complexes using two-dimensional infrared spectroscopy," J. Chem. Phys. **140**, 084505 (2014).
[20]M. Khalil and A. Tokmakoff, "Signatures of vibrational interactions in coherent two-dimensional infrared spectroscopy," J. Chem. Phys. **266**, 213–230 (2001).
[21]M. Khalil, N. Demirdöven, and A. Tokmakoff, "Coherent 2D IR spectroscopy: Molecular structure and dynamics in solution," J. Phys. Chem. A **107**, 5258–5279 (2003).
[22]E. C. Fulmer, P. Mukherjee, A. T. Krummel, and M. T. Zanni, "A pulse sequence for directly measuring the anharmonicities of coupled vibrations: Two-quantum two-dimensional infrared spectroscopy," J. Chem. Phys. **120**, 8067–8078 (2004).
[23]T. A. Oudenhoven, Y. Joo, J. E. Laaser, P. Gopalan, and M. T. Zanni, "Dye aggregation identified by vibrational coupling using 2D IR spectroscopy," J. Chem. Phys. **142**, 212449 (2015).
[24]J. D. Eaves, J. J. Loparo, C. J. Fecko, S. T. Roberts, A. Tokmakoff, and P. L. Geissler, "Hydrogen bonds in liquid water are broken only fleetingly," Proc. Natl. Acad. Sci. U. S. A. **102**, 13019–13022 (2005).
[25]S. T. Roberts, J. J. Loparo, and A. Tokmakoff, "Characterization of spectral diffusion from two-dimensional line shapes," J. Chem. Phys. **125**, 084502 (2006).
[26]T. Brinzer, E. J. Berquist, Z. Ren, S. Dutta, C. A. Johnson, C. S. Krisher, D. S. Lambrecht, and S. Garrett-Roe, "Ultrafast vibrational spectroscopy (2D-IR) of $CO_2$ in ionic liquids: Carbon capture from carbon dioxide's point of view," J. Chem. Phys. **142**, 212425 (2015).
[27]M. L. Cowan, B. D. Bruner, N. Huse, J. R. Dwyer, B. Chugh, E. T. J. Nibbering, T. Elsaesser, and R. J. D. Miller, "Ultrafast memory loss and energy redistribution in the hydrogen bond network of liquid $H_2O$," Nature **434**, 199–202 (2005).
[28]S. Garrett-Roe, F. Perakis, F. Rao, and P. Hamm, "Three-dimensional infrared spectroscopy of isotope-substituted liquid water reveals heterogeneous dynamics," J. Phys. Chem. B **115**, 6976–6984 (2011).
[29]M. C. Thielges and M. D. Fayer, "Protein dynamics studied with ultrafast two-dimensional infrared vibrational echo spectroscopy," Acc. Chem. Res. **45**, 1866–1874 (2012).
[30]E. R. Andresen and P. Hamm, "Site-specific difference 2D-IR spectroscopy of bacteriorhodopsin," J. Phys. Chem. B **113**, 6520–6527 (2009).
[31]S. Woutersen, Y. Mu, G. Stock, and P. Hamm, "Subpicosecond conformational dynamics of small peptides probed by two-dimensional vibrational spectroscopy," Proc. Natl. Acad. Sci. U. S. A. **98**, 11254–11258 (2001).

[32]M. Lim, P. Hamm, and R. M. Hochstrasser, "Protein fluctuations are sensed by stimulated infrared echoes of the vibrations of carbon monoxide and azide probes," Proc. Natl. Acad. Sci. U. S. A. **95**, 15315–15320 (1998).
[33]H. T. Kratochvil, M. Maj, K. Matulef, A. W. Annen, J. Ostmeyer, E. Perozo, B. Roux, F. I. Valiyaveetil, and M. T. Zanni, "Probing the effects of gating on the ion occupancy of the $K^+$ channel selectivity filter using two-dimensional infrared spectroscopy," J. Am. Chem. Soc. **139**, 8837–8845 (2017).
[34]C. R. Baiz, Y.-S. Lin, C. S. Peng, K. A. Beauchamp, V. A. Voelz, V. S. Pande, and A. Tokmakoff, "A molecular interpretation of 2D IR protein folding experiments with Markov state models," Biophys. J. **106**, 1359–1370 (2014).
[35]P. Hamm and M. T. Zanni, *Concepts and Methods of 2D Infrafred Spectroscopy* (Cambridge University Press, 2011).
[36]A. Tokmakoff, "Orientational correlation functions and polarization selectivity for nonlinear spectroscopy of isotropic media. I. Third order," J. Chem. Phys. **105**, 1–12 (1996).
[37]E. L. Read, G. S. Engel, T. R. Calhoun, T. Mancal, T. K. Ahn, R. E. Blankenship, and G. R. Fleming, "Cross-peak-specific two-dimensional electronic spectroscopy," Proc. Natl. Acad. Sci. U. S. A. **104**, 14203–14208 (2007).
[38]M. T. Zanni, N.-H. Ge, Y. S. Kim, and R. M. Hochstrasser, "Two-dimensional IR spectroscopy can be designed to eliminate the diagonal peaks and expose only the crosspeaks needed for structure determination," Proc. Natl. Acad. Sci. U. S. A. **98**, 11265–11270 (2001).
[39]E. Thyrhaug, K. Žídek, J. Dostál, D. Bína, and D. Zigmantas, "Exciton structure and energy transfer in the Fenna–Matthews–Olson complex," J. Phys. Chem. Lett. **7**, 1653–1660 (2016).
[40]V. Tiwari, W. K. Peters, and D. M. Jonas, "Electronic resonance with anti-correlated pigment vibrations drives photosynthetic energy transfer outside the adiabatic framework," Proc. Natl. Acad. Sci. U. S. A. **110**, 1203–1208 (2013).
[41]D. M. Jonas, "Vibrational and nonadiabatic coherence in 2D electronic spectroscopy, the Jahn–Teller effect, and energy transfer," Annu. Rev. Phys. Chem. **69**, 327–352 (2018).
[42]O. Golonzka and A. Tokmakoff, "Polarization-selective third-order spectroscopy of coupled vibronic states," J. Chem. Phys. **115**, 297–309 (2001).
[43]S. Woutersen and P. Hamm, "Structure determination of trialanine in water using polarization sensitive two-dimensional vibrational spectroscopy," J. Phys. Chem. B **104**, 11316–11320 (2000).
[44]M. T. Zanni, S. Gnanakaran, J. Stenger, and R. M. Hochstrasser, "Heterodyned two-dimensional infrared spectroscopy of solvent-dependent conformations of acetylproline-$NH_2$," J. Phys. Chem. B **105**, 6520–6535 (2001).
[45]L. De Marco, W. Carpenter, H. Liu, R. Biswas, J. M. Bowman, and A. Tokmakoff, "Differences in the vibrational dynamics of $H_2O$ and $D_2O$: Observation of symmetric and antisymmetric stretching vibrations in heavy water," J. Phys. Chem. Lett. **7**, 1769–1774 (2016).
[46]M. Ji, M. Odelius, and K. J. Gaffney, "Large angular jump mechanism observed for hydrogen bond exchange in aqueous perchlorate solution," Science **328**, 1003–1005 (2010).
[47]P. L. Kramer, J. Nishida, C. H. Giammanco, A. Tamimi, and M. D. Fayer, "Observation and theory of reorientation-induced spectral diffusion in polarization-selective 2D IR spectroscopy," J. Chem. Phys. **142**, 184505 (2015).
[48]L. P. Deflores, Z. Ganim, R. A. Nicodemus, and A. Tokmakoff, "Amide I′–II′ 2D IR spectroscopy provides enhanced protein secondary structural sensitivity," J. Am. Chem. Soc. **131**, 3385–3391 (2009).
[49]T. A. A. Oliver, N. H. C. Lewis, and G. R. Fleming, "Correlating the motion of electrons and nuclei with two-dimensional electronic-vibrational spectroscopy," Proc. Natl. Acad. Sci. U. S. A. **111**, 10061–10066 (2014).
[50]T. L. Courtney, Z. W. Fox, K. M. Slenkamp, and M. Khalil, "Two-dimensional vibrational-electronic spectroscopy," J. Chem. Phys. **143**, 154201 (2015).
[51]J. D. Gaynor, T. L. Courtney, M. Balasubramanian, and M. Khalil, "Fourier transform two-dimensional electronic-vibrational spectroscopy using an octave-spanning mid-IR probe," Opt. Lett. **41**, 2895 (2016).
[52]Y. Song, A. Konar, R. Sechrist, V. P. Roy, R. Duan, J. Dziurgot, V. Policht, Y. A. Matutes, K. J. Kubarych, and J. P. Ogilvie, "Multispectral multidimensional spectrometer spanning the ultraviolet to the mid-infrared," Rev. Sci. Instrum. **90**, 013108 (2019).
[53]J. D. Gaynor and M. Khalil, "Signatures of vibronic coupling in two-dimensional electronic-vibrational and vibrational-electronic spectroscopies," J. Chem. Phys. **147**, 094202 (2017).
[54]J. D. Gaynor, A. Petrone, X. Li, and M. Khalil, "Mapping vibronic couplings in a solar cell dye with polarization-selective two-dimensional electronic-vibrational spectroscopy," J. Phys. Chem. Lett. **9**, 6289–6295 (2018).
[55]J. D. Gaynor, J. Sandwisch, and M. Khalil, "Vibronic coherence evolution in multidimensional ultrafast photochemical processes," Nat. Commun. **10**, 5621 (2019).
[56]T. L. Courtney, Z. W. Fox, L. Estergreen, and M. Khalil, "Measuring coherently coupled intramolecular vibrational and charge-transfer dynamics with two-dimensional vibrational-electronic spectroscopy," J. Phys. Chem. Lett. **6**, 1286–1292 (2015).
[57]Z. W. Fox, T. J. Blair, and M. Khalil, "Determining the orientation and vibronic couplings between electronic and vibrational coordinates with polarization-selective two-dimensional vibrational-electronic spectroscopy," J. Phys. Chem. Lett. **11**, 1558–1563 (2020).
[58]P. P. Roy, J. Shee, E. A. Arsenault, Y. Yoneda, K. Feuling, M. Head-Gordon, and G. R. Fleming, "Solvent mediated excited state proton transfer in indigo carmine," J. Phys. Chem. Lett. **11**, 4156–4162 (2020).
[59]N. H. C. Lewis and G. R. Fleming, "Two-dimensional electronic-vibrational spectroscopy of chlorophyll *a* and *b*," J. Phys. Chem. Lett. **7**, 831–837 (2016).
[60]E. A. Arsenault, Y. Yoneda, M. Iwai, K. K. Niyogi, and G. R. Fleming, "The role of mixed vibronic $Q_y$-$Q_x$ states in green light absorption of light-harvesting complex II," Nat. Commun. **11**, 6011 (2020).
[61]E. A. Arsenault, Y. Yoneda, M. Iwai, K. K. Niyogi, and G. R. Fleming, "Vibronic mixing enables ultrafast energy flow in light-harvesting complex II," Nat. Commun. **11**, 1460 (2020).
[62]N. H. C. Lewis, N. L. Gruenke, T. A. A. Oliver, M. Ballottari, R. Bassi, and G. R. Fleming, "Observation of electronic excitation transfer through light harvesting complex II using two-dimensional electronic-vibrational spectroscopy," J. Phys. Chem. Lett. **7**, 4197–4206 (2016).
[63]T. A. A. Oliver and G. R. Fleming, "Following coupled electronic-nuclear motion through conical intersections in the ultrafast relaxation of β-Apo-8′-carotenal," J. Phys. Chem. B **119**, 11428–11441 (2015).
[64]E. C. Wu, Q. Ge, E. A. Arsenault, N. H. C. Lewis, N. L. Gruenke, M. J. Head-Gordon, and G. R. Fleming, "Two-dimensional electronic-vibrational spectroscopic study of conical intersection dynamics: An experimental and electronic structure study," Phys. Chem. Chem. Phys. **21**, 14153–14163 (2019).
[65]P. Bhattacharyya and G. R. Fleming, "Two-dimensional electronic-vibrational spectroscopy of coupled molecular complexes: A near-analytical approach," J. Phys. Chem. Lett. **10**, 2081–2089 (2019).
[66]N. H. C. Lewis, H. Dong, T. A. A. Oliver, and G. R. Fleming, "Measuring correlated electronic and vibrational spectral dynamics using line shapes in two-dimensional electronic-vibrational spectroscopy," J. Chem. Phys. **142**, 174202 (2015).
[67]H. Dong, N. H. C. Lewis, T. A. A. Oliver, and G. R. Fleming, "Determining the static electronic and vibrational energy correlations via two-dimensional electronic-vibrational spectroscopy," J. Chem. Phys. **142**, 174201 (2015).
[68]M. Cho and G. R. Fleming, "Two-dimensional electronic-vibrational spectroscopy reveals cross-correlation between solvation dynamics and vibrational spectral diffusion," J. Phys. Chem. B **124**, 11222–11235 (2020).
[69]Y. Song, A. Schubert, E. Maret, R. K. Burdick, B. D. Dunietz, E. Geva, and J. P. Ogilvie, "Vibronic structure of photosynthetic pigments probed by polarized two-dimensional electronic spectroscopy and *ab initio* calculations," Chem. Sci. **10**, 8143–8153 (2019).
[70]V. Tiwari, W. K. Peters, and D. M. Jonas, "Electronic energy transfer through non-adiabatic vibrational-electronic resonance. I. Theory for a dimer," J. Chem. Phys. **147**, 154308 (2017).
[71]V. Tiwari and D. M. Jonas, "Electronic energy transfer through non-adiabatic vibrational-electronic resonance. II. 1D spectra for a dimer," J. Chem. Phys. **148**, 084308 (2018).
[72]G. M. Sando, K. G. Spears, J. T. Hupp, and P. T. Ruhoff, "Large electron transfer rate effects from the Duschinsky mixing of vibrations," J. Phys. Chem. A **105**, 5317–5325 (2001).

[73]J. W. Kim, J. Jeon, T. H. Yoon, and M. Cho, "Two-dimensional electronic spectroscopy of bacteriochlorophyll a with synchronized dual mode-locked lasers," Nat. Commun. **11**, 6029 (2020).
[74]H.-D. Zhang, Q. Qiao, R.-X. Xu, and Y. Yan, "Effects of Herzberg–Teller vibronic coupling on coherent excitation energy transfer," J. Chem. Phys. **145**, 204109 (2016).
[75]L. Paul, T. Moitra, K. Ruud, and S. Chakrabarti, "Strong Duschinsky mixing induced breakdown of Kasha's rule in an organic phosphor," J. Phys. Chem. Lett. **10**, 369–374 (2019).
[76]R. B. Weakly, J. D. Gaynor, and M. Khalil, "Multimode two-dimensional vibronic spectroscopy. II. Simulating and extracting vibronic coupling parameters from polarization-selective spectra," J. Chem. Phys. **154**, 184202 (2021).
[77]K. Huang and A. Rhys, "Theory of light absorption and non-radiative transitions in F-centres," Proc. R. Soc., A **204**, 406–423 (1950).
[78]S. Mukamel, *Principles of Nonlinear Optical Spectroscopy* (Oxford University Press, New York, 1995).
[79]J. Sung and R. J. Silbey, "Four wave mixing spectroscopy for a multilevel system," J. Chem. Phys. **115**, 9266–9287 (2001).
[80]M. Cho, G. R. Fleming, and S. Mukamel, "Nonlinear response functions for birefringence and dichroism measurements in condensed phases," J. Chem. Phys. **98**, 5314–5326 (1993).
[81]B. J. Berne and R. Pecora, *Dynamic Light Scattering: With Applications in Chemistry, Biology, and Physics* (Dover, New York, 2000).
[82]L. D. Favro, "Theory of the rotational Brownian motion of a free rigid body," Phys. Rev. **119**, 53–62 (1960).
[83]C. C. Wang and R. Pecora, "Time-correlation functions for restricted rotational diffusion," J. Chem. Phys. **72**, 5333–5340 (1980).
[84]M. Khalil, N. Demirdöven, and A. Tokmakoff, "Vibrational coherence transfer characterized with Fourier-transform 2D IR spectroscopy," J. Chem. Phys. **121**, 362–373 (2004).
[85]R. M. Hochstrasser, "Two-dimensional IR-spectroscopy: Polarization anisotropy effects," Chem. Phys. **266**, 273–284 (2001).
[86]J. R. Lakowicz, *Principles of Fluorescence Spectroscopy* (Springer US, New York, 2006).
[87]M. Lim, T. Jackson, and P. Anfinrud, "Binding of CO to myoglobin from a heme pocket docking site to form nearly linear Fe–C–O," Science **269**, 962–966 (1995).
[88]M. S. Lynch, K. M. Slenkamp, M. Cheng, and M. Khalil, "Coherent fifth-order visible-infrared spectroscopies: Ultrafast nonequilibrium vibrational dynamics in solution," J. Phys. Chem. A **116**, 7023–7032 (2012).
[89]C. R. Baiz, R. McCanne, M. J. Nee, and K. J. Kubarych, "Orientational dynamics of transient molecules measured by nonequilibrium two-dimensional infrared spectroscopy," J. Phys. Chem. A **113**, 8907–8916 (2009).
[90]J. Bredenbeck, J. Helbing, and P. Hamm, "Transient two-dimensional infrared spectroscopy: Exploring the polarization dependence," J. Chem. Phys. **121**, 5943–5957 (2004).
[91]G. S. Schlau-Cohen, T. R. Calhoun, N. S. Ginsberg, M. Ballottari, R. Bassi, and G. R. Fleming, "Spectroscopic elucidation of uncoupled transition energies in the major photosynthetic light-harvesting complex, LHCII," Proc. Natl. Acad. Sci. U. S. A. **107**, 13276–13281 (2010).
[92]D. Paleček, P. Edlund, E. Gustavsson, S. Westenhoff, and D. Zigmantas, "Potential pitfalls of the early-time dynamics in two-dimensional electronic spectroscopy," J. Chem. Phys. **151**, 024201 (2019).
[93]M. K. Petti, J. S. Ostrander, E. R. Birdsall, M. B. Kunz, Z. T. Armstrong, A. M. Alperstein, and M. T. Zanni, "A proposed method to obtain surface specificity with pump-probe and 2D spectroscopies," J. Phys. Chem. A **124**, 3471–3483 (2020).
[94]J. A. Myers, K. L. Lewis, P. F. Tekavec, and J. P. Ogilvie, "Two-color two-dimensional Fourier transform electronic spectroscopy with a pulse-shaper," Opt. Express **16**, 17420 (2008).
[95]Z. W. Fox, T. J. Blair, R. B. Weakly, T. L. Courtney, and M. Khalil, "Implementation of continuous fast scanning detection in femtosecond Fourier-transform two-dimensional vibrational-electronic spectroscopy to decrease data acquisition time," Rev. Sci. Instrum. **89**, 113104 (2018).